

Contents

1	Introduction	1
1.1	A Brief History of Seismology	2
1.2	EXERCISES	13
2	Stress and Strain	17
2.1	The Stress Tensor	17
2.1.1	Example: Computing the traction vector	19
2.1.2	Principal axes of stress	19
2.1.3	Example: Computing the principal axes	21
2.1.4	Deviatoric stress	22
2.1.5	Values for stress	23
2.2	The Strain Tensor	23
2.2.1	Values for strain	27
2.2.2	Example: Computing strain for a seismic wave	27
2.3	The Linear Stress–Strain Relationship	27
2.3.1	Units for elastic moduli	30
2.4	EXERCISES	30
3	The Seismic Wave Equation	37
3.1	Introduction: The Wave Equation	37
3.2	The Momentum Equation	38
3.3	The Seismic Wave Equation	40
3.3.1	Potentials	42
3.4	Plane Waves	43
3.4.1	Example: Harmonic plane wave equation	44
3.5	Polarizations of P and S Waves	44
3.6	Spherical Waves	45
3.7	Methods for Computing Synthetic Seismograms [†]	47
3.8	The Future of Seismology? [†]	49
3.9	Equations for 2-D Isotropic Finite Differences [†]	52
3.10	EXERCISES	56

4	Ray Theory: Travel Times	59
4.1	Snell's Law	59
4.2	Ray Paths for Laterally Homogeneous Models	61
4.2.1	Example: Computing $X(p)$ and $T(p)$	63
4.2.2	Ray tracing through velocity gradients	64
4.3	Travel Time Curves and Delay Times	65
4.3.1	Reduced velocity	66
4.3.2	The $\tau(p)$ function	66
4.4	Low Velocity Zones	68
4.5	Summary of 1-D Ray Tracing Equations	69
4.6	Spherical Earth Ray Tracing	70
4.7	The Earth-Flattening Transformation	73
4.8	Three-Dimensional Ray Tracing [†]	74
4.9	Ray Nomenclature	76
4.9.1	Crustal phases	76
4.9.2	Whole Earth phases	77
4.9.3	<i>PKJKP</i> : The Holy Grail of body wave seismology	78
4.10	Global Body Wave Observations	79
4.11	EXERCISES	88
5	Inversion of Travel Time Data	93
5.1	One-Dimensional Velocity Inversion	93
5.2	Straight-Line Fitting	96
5.2.1	Example: Solving for a layer cake model	98
5.2.2	Other ways to fit the $T(X)$ curve	98
5.3	$\tau(p)$ Inversion	99
5.3.1	Example: The layer cake model revisited	100
5.4	Linear Programming and Regularization Methods	103
5.5	Summary: One-Dimensional Velocity Inversion	105
5.6	Three-Dimensional Velocity Inversion	106
5.6.1	Setting up the tomography problem	106
5.6.2	Solving the tomography problem	110
5.6.3	Tomography complications	111
5.6.4	Finite frequency tomography	112
5.7	Earthquake Location	114
5.7.1	Iterative location methods	119
5.7.2	Relative event location methods	120
5.8	EXERCISES	121
6	Ray Theory: Amplitude and Phase	125
6.1	Energy in Seismic Waves	125
6.2	Geometrical Spreading in 1-D Velocity Models	127
6.3	Reflection and Transmission Coefficients	129
6.3.1	SH-Wave reflection and transmission coefficients	130

6.3.2	Example: Computing SH coefficients	133
6.3.3	Vertical incidence coefficients	134
6.3.4	Energy-normalized coefficients	135
6.3.5	Dependence on ray angle	136
6.4	Turning Points and Hilbert Transforms	139
6.5	Matrix Methods for Modeling Plane Waves [†]	142
6.6	Attenuation	146
6.6.1	Example: Computing intrinsic attenuation	147
6.6.2	t^* and velocity dispersion	147
6.6.3	The absorption band model [†]	149
6.6.4	The standard linear solid [†]	152
6.6.5	Earth's attenuation	154
6.6.6	Observing Q	156
6.6.7	Non-linear attenuation	157
6.6.8	Seismic attenuation and global politics	157
6.7	EXERCISES	158
7	Reflection Seismology	161
7.1	Zero-Offset Sections	162
7.2	Common Midpoint Stacking	164
7.3	Sources and Deconvolution	167
7.4	Migration	170
7.4.1	Huygens' principle	171
7.4.2	Diffraction hyperbolas	172
7.4.3	Migration methods	173
7.5	Velocity Analysis	175
7.5.1	Statics corrections	176
7.6	Receiver Functions	176
7.7	Kirchhoff Theory [†]	180
7.7.1	Kirchhoff applications	184
7.7.2	How to write a Kirchhoff program	186
7.7.3	Kirchhoff migration	187
7.8	EXERCISES	187
8	Surface Waves and Normal Modes	191
8.1	Love Waves	191
8.1.1	Solution for a single layer	194
8.2	Rayleigh Waves	195
8.3	Dispersion	198
8.4	Global Surface Waves	200
8.5	Observing Surface Waves	202
8.6	Normal Modes	205
8.7	EXERCISES	211

9	Earthquakes and Source Theory	215
9.1	Green's Functions and the Moment Tensor	215
9.2	Earthquake Faults	219
9.2.1	Non-double-couple sources	222
9.3	Radiation Patterns and Beach Balls	224
9.3.1	Example: Plotting a focal mechanism	231
9.4	Far-Field Pulse Shapes	232
9.4.1	Directivity	234
9.4.2	Source spectra	236
9.4.3	Empirical Green's functions	238
9.5	Stress Drop	239
9.5.1	Self-similar earthquake scaling	242
9.6	Radiated Seismic Energy	243
9.6.1	Earthquake energy partitioning	246
9.7	Earthquake Magnitude	249
9.7.1	The b -value	256
9.7.2	The intensity scale	257
9.8	Finite Slip Modeling	259
9.9	The Heat Flow Paradox	261
9.10	EXERCISES	263
10	Earthquake Prediction	267
10.1	The Earthquake Cycle	267
10.2	Earthquake Triggering	274
10.3	Searching for Precursors	279
10.4	Are Earthquakes Unpredictable?	281
10.5	EXERCISES	282
11	Instruments, Noise, and Anisotropy	285
11.1	Instruments	285
11.1.1	Modern seismographs	290
11.2	Earth Noise	293
11.3	Anisotropy [†]	295
11.3.1	Snell's Law at an interface	299
11.3.2	Weak anisotropy	299
11.3.3	Shear-wave splitting	301
11.3.4	Hexagonal anisotropy	302
11.3.5	Mechanisms for anisotropy	304
11.3.6	Earth's anisotropy	305
11.4	EXERCISES	307
A	The PREM Model	311

B Math Review	315
B.1 Vector Calculus	315
B.2 Complex Numbers	319
C The Eikonal Equation	323
D Fortran Subroutines	327
E Time Series and Fourier Transforms	333
E.1 Convolution	333
E.2 Fourier Transform	334
E.3 Hilbert Transform	335

Chapter 1

Introduction

Every day there are about fifty earthquakes worldwide that are strong enough to be felt locally, and every few days an earthquake occurs that is capable of damaging structures. Each event radiates seismic waves that travel throughout Earth, and several earthquakes per day produce distant ground motions that, although too weak to be felt, are readily detected with modern instruments anywhere on the globe. Seismology is the science that studies these waves and what they tell us about the structure of Earth and the physics of earthquakes. It is the primary means by which scientists learn about Earth's deep interior, where direct observations are impossible, and has provided many of the most important discoveries regarding the nature of our planet. It is also directly concerned with understanding the physical processes that cause earthquakes and seeking ways to reduce their destructive impacts on humanity.

Seismology occupies an interesting position within the more general fields of geophysics and Earth sciences. It presents fascinating theoretical problems involving analysis of elastic wave propagation in complex media, but it can also be applied simply as a tool to examine different areas of interest. Applications range from studies of Earth's core, thousands of kilometers below the surface, to detailed mapping of shallow crustal structure to help locate petroleum deposits. Much of the underlying physics is no more advanced than Newton's second law ($F = ma$), but the complications introduced by realistic sources and structures have motivated sophisticated mathematical treatments and extensive use of powerful computers. Seismology is driven by observations, and improvements in instrumentation and data availability have often led to breakthroughs both in seismology theory and our understanding of Earth structure.

The information that seismology provides has widely varying degrees of uncertainty. Some parameters, such as the average compressional wave travel time through the mantle, are known to a fraction of a percent, while others, such as the degree of damping of seismic energy within the inner core, are known only very approximately. The average radial seismic velocity structure of Earth has been known fairly well for over fifty years, and the locations and seismic radiation patterns of earthquakes are now routinely mapped, but many important aspects of the physics

of earthquakes themselves remain a mystery.

1.1 A Brief History of Seismology

Seismology is a comparatively young science that has only been studied quantitatively for about 100 years. Reviews of the history of seismology include Dewey and Byerly (1969) and Agnew (2002). Early thinking about earthquakes was, as one might expect, superstitious and not very scientific. It was noted that earthquakes and volcanoes tended to go together, and explanations for earthquakes involving underground explosions were common. In the early 1800s the theory of elastic wave propagation began to be developed by Cauchy, Poisson, Stokes, Rayleigh, and others who described the main wave types to be expected in solid materials. These include compressional and shear waves, termed *body waves* since they travel through solid volumes, and *surface waves*, which travel along free surfaces. Since compressional waves travel faster than shear waves and arrive first, they are often called primary or *P*-waves, whereas the later arriving shear waves are called secondary or *S*-waves. At this time theory was ahead of seismic observations, since these waves were not identified in Earth until much later.

In 1857 a large earthquake struck near Naples. Robert Mallet, an Irish engineer interested in quakes, traveled to Italy to study the destruction caused by the event. His work represented the first significant attempt at observational seismology and described the idea that earthquakes radiate seismic waves away from a focus point (now called the *hypocenter*) and that they can be located by projecting these waves backward to the source. Mallet's analysis was flawed since he assumed that earthquakes are explosive in origin and only generate compressional waves. Nevertheless, his general concept was sound, as were his suggestions that observatories be established to monitor earthquakes and his experiments on measuring seismic velocities using artificial sources.

Early seismic instrumentation was based on undamped pendulums, which did not continuously record time, although sometimes an onset time was measured. The first time-recording seismograph was built in Italy by Filippo Cecchi in 1875. Soon after this, higher quality instruments were developed by the British in Japan, beginning with a horizontal pendulum design by James Ewing that recorded on a rotating disk of smoked glass. The first observation of a distant earthquake, or *teleseism*, was made in Potsdam in 1889 for a Japanese event. In 1897 the first North American seismograph was installed at Lick Observatory near San Jose in California; this device was later to record the 1906 San Francisco earthquake. These early instruments were undamped, and they could provide accurate estimates of ground motion only for a short time at the beginning of shaking. In 1898 E. Wiechert introduced the first seismometer with viscous damping, capable of producing useful records for the entire duration of an earthquake. The first electromagnetic seismographs, in which a moving pendulum is used to generate an electric current in a coil, were developed in the early 1900s, by B. B. Galitzen, who established a chain of stations across

Russia. All modern seismographs are electromagnetic, since these instruments have numerous advantages over the purely mechanical designs of the earliest instruments.

The availability of seismograms recorded at a variety of ranges from earthquakes led to rapid progress in determining Earth's seismic velocity structure. By 1900 Richard Oldham reported the identification of P -, S -, and surface waves on seismograms, and later (1906) he detected the presence of Earth's core from the absence of direct P and S arrivals at source–receiver distances beyond about 100° . In 1909 Andrija Mohorovičić reported observations showing the existence of a velocity discontinuity separating the crust and mantle (this interface is now generally referred to, somewhat irreverently, as the “Moho”). Tabulations of arrival times led to the construction of travel time tables (arrival time as a function of distance from the earthquake); the first widely used tables were produced by Zöppritz in 1907. Beno Gutenberg published tables in 1914 with core phases (waves that penetrate or reflect off the core) and reported the first accurate estimate for the depth of Earth's fluid core (2,900 km, very close to the modern value of 2,889 km). In 1936, Inge Lehmann discovered the solid inner core, and in 1940 Harold Jeffreys and K. E. Bullen published the final version of their travel time tables for a large number of seismic phases. The JB tables are still in use today and contain times that differ by only a few seconds from current models.

The travel times of seismic arrivals can be used to determine Earth's average velocity versus depth structure, and this was largely accomplished over fifty years ago. The crust varies from about 6 km in thickness under the oceans to 30–50 km beneath continents. The deep interior is divided into three main layers: the mantle, the outer core, and the inner core (Fig. 1.1). The mantle is the solid rocky outer shell that makes up 84% of our planet's volume and 68% of the mass. It is characterized by a fairly rapid velocity increase in the upper mantle between about 300 and 700 km depth, a region termed the *transition zone*, where several mineralogical phase changes are believed to occur (including those at the 410- and 660-km seismic discontinuities, shown as the dashed arcs in Fig. 1.1). Between about 700 km to near the core–mantle-boundary (CMB), velocities increase fairly gradually with depth; this increase is in general agreement with that expected from the changes in pressure and temperature on rocks of uniform composition and crystal structure.

At the CMB, the P velocity drops dramatically from almost 14 km/s to about 8 km/s and the S velocity goes from about 7 km/s to zero. This change (larger than the velocity contrast at Earth's surface!) occurs at a sharp interface that separates the solid mantle from the fluid outer core. Within the outer core, the P velocity again increases gradually, at a rate consistent with that expected for a well-mixed fluid. However, at a radius of about 1,221 km the core becomes solid, the P velocities increase slightly, and non zero shear velocities are present. Earth's core is believed to be composed mainly of iron and the inner-core boundary (ICB) is thought to represent a phase change in iron to a different crystal structure.

Earth's internal density distribution is much more difficult to determine than the velocity structure, since P and S travel times provide no direct constraints on

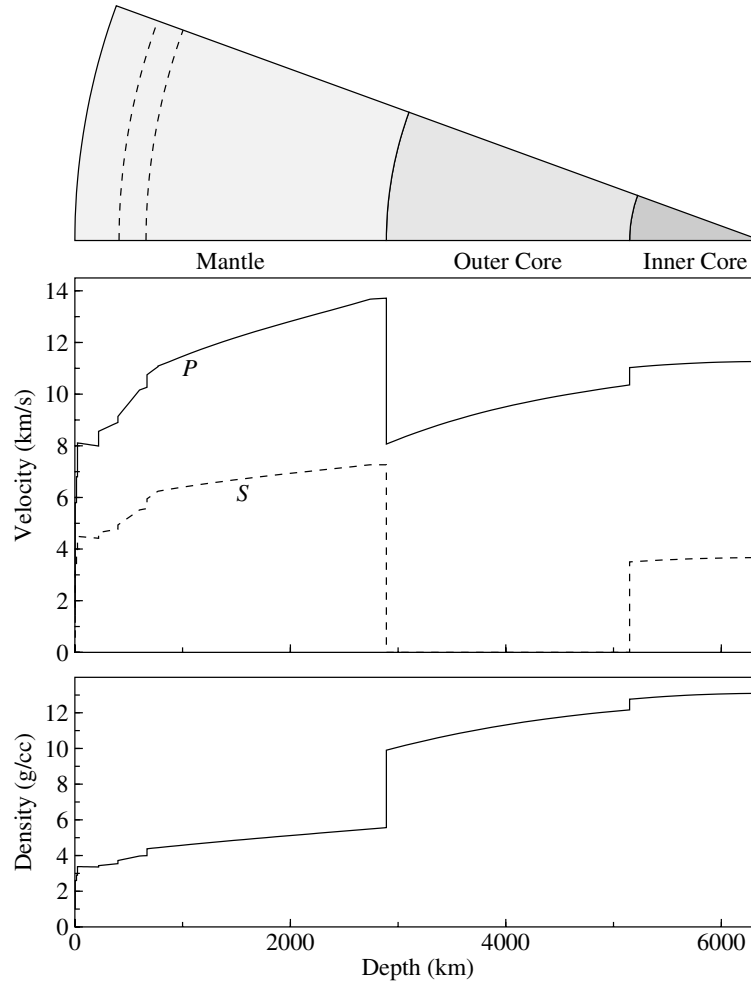


Figure 1.1: Earth's P velocity, S velocity, and density as a function of depth. Values are plotted from the Preliminary Reference Earth Model (PREM) of Dziewonski and Anderson (1981); except for some differences in the upper mantle, all modern Earth models are close to these values. PREM is listed as a table in Appendix 1.

density. However, by using probable velocity versus density scaling relationships and Earth's known mass and moment of inertia, K. E. Bullen showed that it is possible to infer a density profile similar to that shown in Figure 1.1. Modern results from normal mode seismology, which provides more direct constraints on density (although with limited vertical resolution), have generally proven consistent with the older density profiles.

Seismic surveying using explosions and other artificial sources was developed during the 1920s and 1930s for prospecting purposes in the oil producing regions of Mexico and the United States. Early work involved measuring the travel time versus distance of P -waves to determine seismic velocity at depth. Later studies focused on reflections from subsurface layering (reflection seismology), which can achieve high resolution when instruments are closely spaced. The common-midpoint (CMP) stacking method for reflection seismic data was patented in 1956, leading to reduced

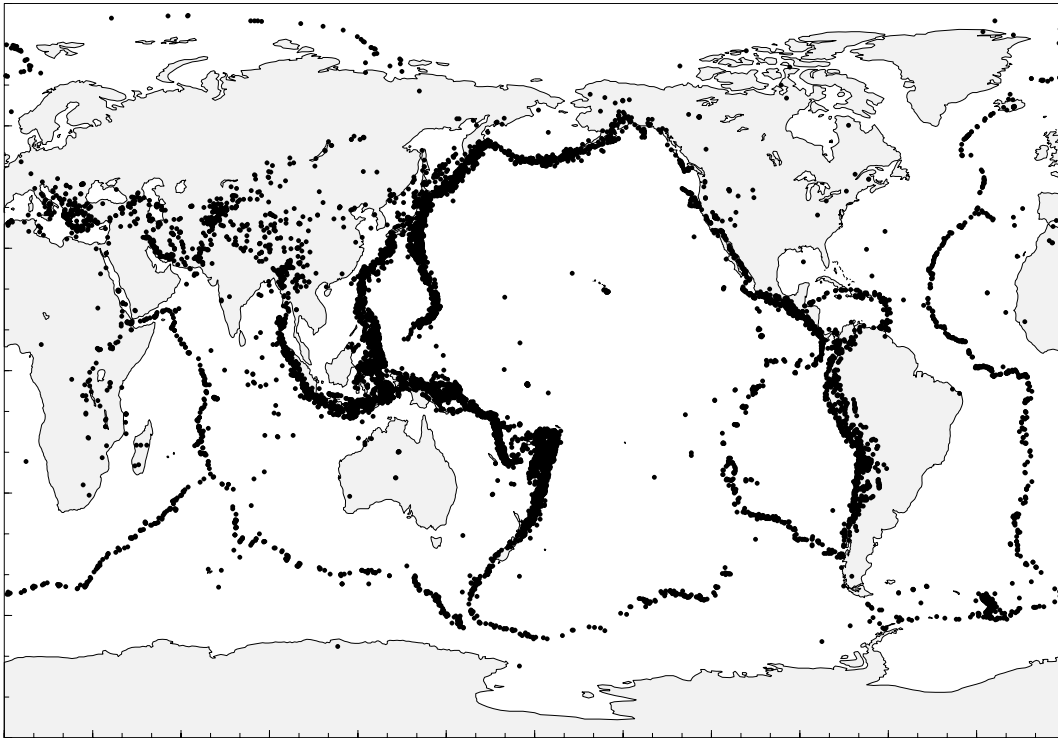


Figure 1.2: Selected global earthquake locations from 1977 to 1994 (taken from the PDE and ISC catalogs). Earthquakes occur along well-defined belts of seismicity; these are particularly prominent around the Pacific rim and along mid-oceanic ridges. We now know that these belts define the edges of the tectonic plates within Earth's rigid outermost layer (see Fig. 1.3).

noise levels and higher-quality profiles. The Vibroseis method, also developed in the 1950s, applies signal-processing techniques to data recorded using a long-duration, vibrating source.

The increasing number of seismic stations established in the early 1900s enabled large earthquakes to be routinely located, leading to the discovery that earthquakes are not randomly distributed but tend to occur along well-defined belts (Fig. 1.2). However, the significance of these belts was not fully appreciated until the 1960s, as part of the plate tectonics revolution in the Earth sciences. At that time, it was recognized that Earth's surface features are largely determined by the motions of a small number of relatively rigid plates that drift slowly over geological time (Fig. 1.3). The relative motions between adjacent plates give rise to earthquakes along the plate boundaries. The plates are spreading apart along the mid-oceanic ridges, where new oceanic lithosphere is being formed. This has caused the splitting apart and separation of Europe and Africa from the Americas (the “continental drift” hypothesized by Alfred Wegener in 1915). The plates are recycled back into the mantle in the trenches and subduction zones around the Pacific margin. Large shear faults, such as the San Andreas Fault in California, are a result of transverse motion between plates. Plate boundaries across continents are often more diffuse and

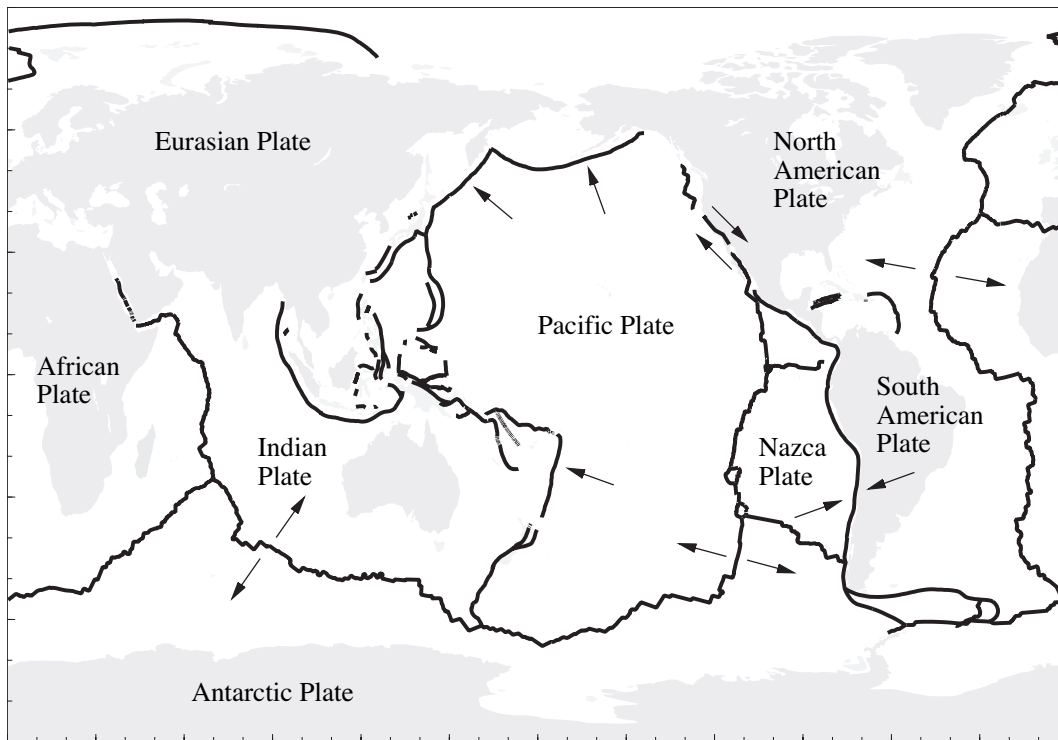


Figure 1.3: Earth's major tectonic plates. The arrows indicate relative plate motions at some of the plate boundaries. The plates are pulling apart along spreading centers, such as the Mid-Atlantic Ridge, where new crust is being formed. Along the subduction zones in the western Pacific, the Pacific Plate is sliding back down into the mantle. The San Andreas Fault in California is a result of shear between the Pacific and North American Plates.

marked by distributed seismicity, such as occurs in the Himalayan region between the northward moving Indian Plate and the Eurasian Plate.

In the 1960s, seismologists were able to show that the *focal mechanisms* (the type of faulting as inferred from the radiated seismic energy) of most global earthquakes are consistent with that expected from plate tectonic theory, thus helping to validate the still emerging paradigm. However, considering the striking similarity between Figures 1.2 and 1.3, why didn't seismologists begin to develop the theory of plate tectonics much earlier? In part, this can be attributed to the lower resolution of the older earthquake locations compared to more modern results. However, a more important reason was that seismologists, like most geophysicists at the time, did not feel that ideas of continental drift had a sound physical basis. Thus they were unable to fully appreciate the significance and implications of the earthquake locations, and tended to interpret their results in terms of local and regional tectonics, rather than a unifying global theory.

In 1923, H. Nakano introduced the theory for the seismic radiation from a double-couple source (for about the next forty years, a controversy would rage over the question of whether a single- or double-couple source is most appropriate for earthquakes, despite the fact that theory shows that single-couple sources are physically impos-

sible). In 1928, Kiyoo Wadati reported the first convincing evidence for deep focus earthquakes (below 100 km depth). A few years earlier, H. H. Turner had located some earthquakes at significant depth, but his analyses were not generally accepted (particularly since he also located some events in the air above the surface!). Deep focus events are typically observed along dipping planes of seismicity (often termed Wadati–Benioff zones) that can extend to almost 700 km depth; these mark the locations of subducting slabs of oceanic lithosphere that are found surrounding much of the Pacific Ocean. Figure 1.4 shows a cross section of the earthquake locations in the Tonga subduction zone in the southwest Pacific, the world’s most active area of deep seismicity. The existence of deep events was a surprising discovery because the high pressures and temperatures that exist at these depths should make most materials deform ductilely, without the sudden brittle failure that causes shallow earthquakes in the crust. Even today the physical mechanism for deep events is not well understood and is a continuing source of controversy.

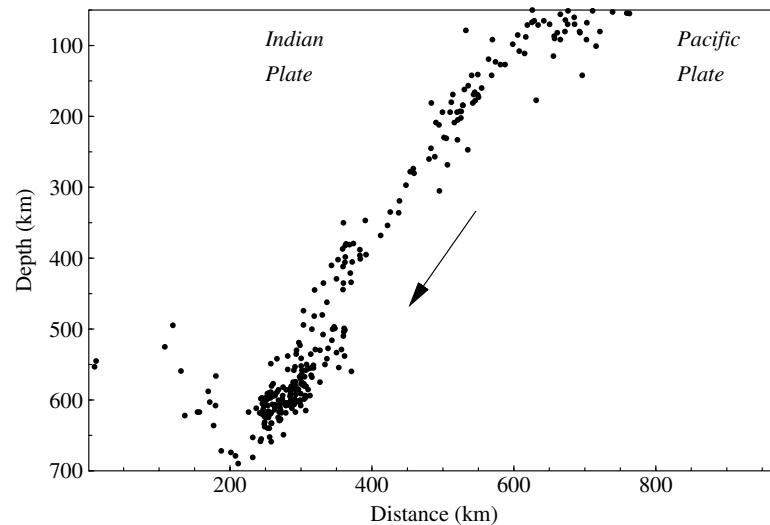


Figure 1.4: A vertical west–east cross section of the deep seismicity in the Tonga subduction zone, showing selected earthquakes from the PDE and ISC catalogs between 1977 and 1994. The seismicity marks where the lithosphere of the Pacific Plate is sinking down into the mantle.

In 1946, an underwater nuclear explosion near Bikini Atoll led to the first detailed seismic recordings of a nuclear bomb. Perhaps a more significant development, at least for western government funding for seismology, was the 1949 testing of a Soviet nuclear bomb. This led to an intense interest by the U.S. military in the ability of seismology to detect nuclear explosions, estimate yields, and discriminate between explosions and earthquakes. A surge in funding for seismology resulted, helping to improve seismic instrumentation and expand government and university seismology programs. In 1961 the Worldwide Standardized Seismograph Network (WWSSN) was established, consisting of well-calibrated instruments with both short- and long-period seismometers. The ready availability of records from these seismographs led to rapid improvements in many areas of seismology, including the production of

much more complete and accurate catalogs of earthquake locations and the long overdue recognition that earthquake radiation patterns are consistent with double-couple sources.

Records obtained from the great Chilean earthquake of 1960 were the first to provide definitive observations of Earth’s *free oscillations*. Any finite solid will resonate only at certain vibration frequencies, and these *normal modes* provide an alternative to the traveling wave representation for characterizing the deformations in the solid. Earth “rings” for several days following large earthquakes, and its normal modes are seen as peaks in the power spectrum of seismograms. The 1960s and 1970s saw the development of the field of normal mode seismology, which gives some of the best constraints on the large-scale structure, particularly in density, of Earth’s interior. Analyses of normal mode data also led to the development of many important ideas in geophysical inverse theory, providing techniques for evaluating the uniqueness and resolution of Earth models obtained from indirect observations.

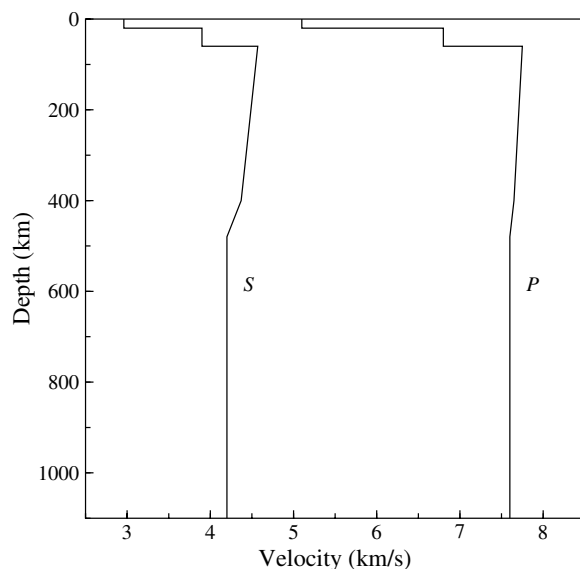


Figure 1.5: An approximate seismic velocity model derived for the Moon from observations of quakes and surface impacts (from Goins et al., 1981). Velocities at greater depths (the lunar radius is 1,737 km) are largely unconstrained owing to a lack of deep seismic waves in the *Apollo* data set.

Between 1969 and 1972, seismometers were placed on the Moon by the Apollo astronauts and the first lunar quakes were recorded. These include surface impacts, shallow quakes within the top 100 km, and deeper quakes at roughly 800 to 1,000 km depth. Lunar seismograms appear very different from those on Earth, with lengthy wavetrains of high-frequency scattered energy. This has complicated their interpretation, but a lunar crust and mantle have been identified, with a crustal thickness of about 60 km (see Fig. 1.5). A seismometer placed on Mars by the *Viking 2* probe in 1976 was hampered by wind noise and only one possible Mars quake was identified.

Although it is not practical to place seismometers on the Sun, it is possible to

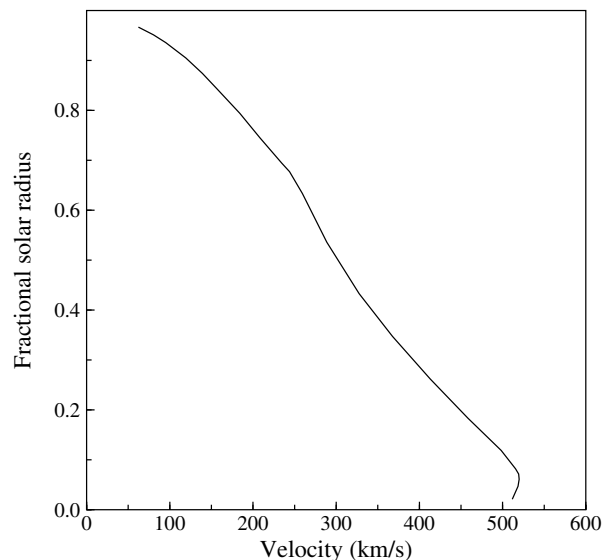


Figure 1.6: The velocity of sound within the Sun (adapted from Harvey, 1995).

detect oscillations of the solar surface by measuring the Doppler shift of spectral lines. Such oscillations were first observed in 1960 by Robert Leighton, who discovered that the Sun's surface vibrates continually at a period of about five minutes and is incoherent over small spatial wavelengths. These oscillations were initially interpreted as resulting from localized gas movements near the solar surface, but in the late 1960s several researchers proposed that the oscillations resulted from acoustic waves trapped within the Sun. This idea was confirmed in 1975 when it was shown that the pattern of observed vibrations is consistent with that predicted for the free oscillations of the Sun, and the field of *helioseismology* was born. Analysis is complicated by the fact that, unlike Earth, impulsive sources analogous to earthquakes are rarely observed; the excitation of acoustic energy is a continuous process. However, many of the analysis techniques developed for normal mode seismology can be applied, and the radial velocity structure of the Sun is now well constrained (Fig. 1.6). Continuing improvements in instrumentation and dedicated experiments promise further breakthroughs, including resolution of spatial and temporal variations in solar velocity structure. In only a few decades, helioseismology has become one of the most important tools for examining the structure of the Sun.

The advent of computers in the 1960s changed the nature of terrestrial seismology, by enabling analyses of large data sets and more complicated problems, and led to the routine calculation of earthquake locations. The first complete theoretical seismograms for complicated velocity structures began to be computed at this time. The computer era also has seen the rapid expansion of seismic imaging techniques using artificial sources that have been applied extensively by the oil industry to map shallow crustal structure. Beginning in 1976, data started to become available from global seismographs in digital form, greatly facilitating quantitative waveform comparisons. In recent years, many of the global seismic stations have been upgraded to

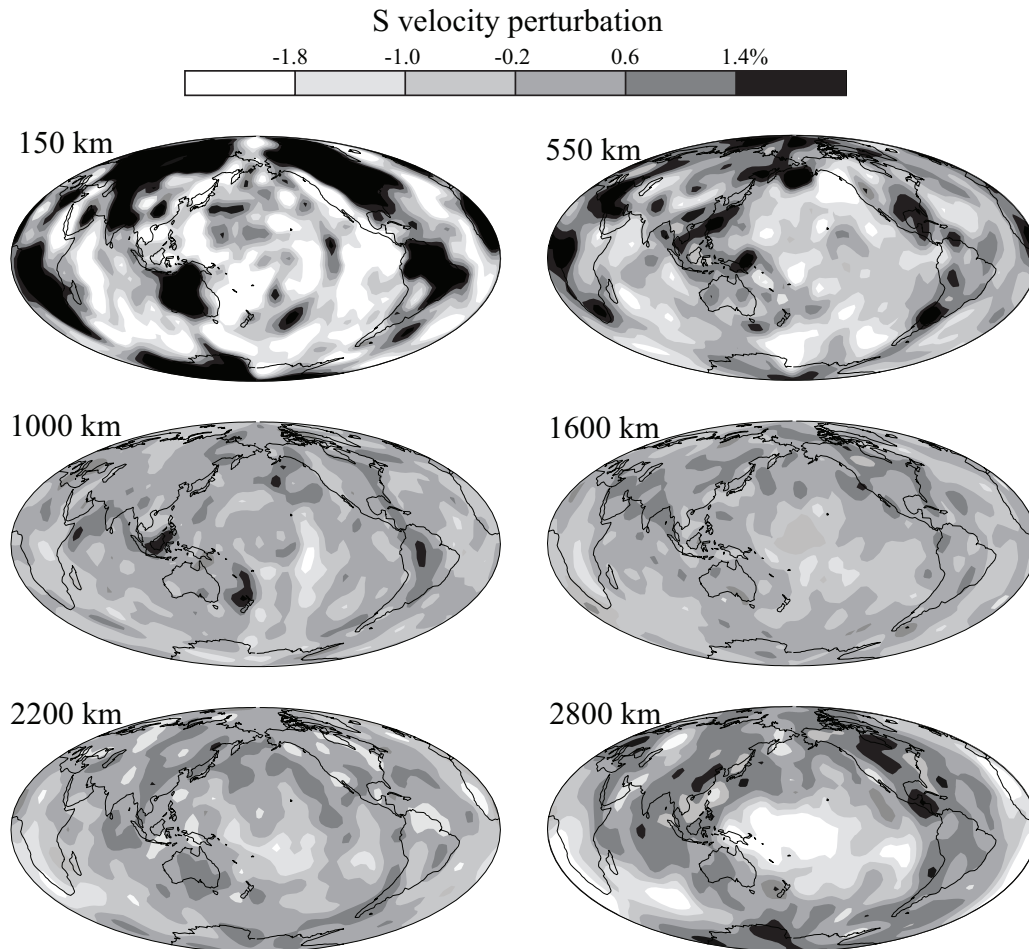


Figure 1.7: Lateral variations in S velocity at depths of 150, 550, 1000, 1600, 2200, and 2800 km in the mantle from Manners and Masters (2008). Velocity perturbations are contoured as shown, with black indicating regions that are more than 1.4% faster than average, and white indicating velocities over 1.8% slower than average.

broadband, high dynamic range seismometers, and new instruments have been deployed to fill in gaps in the global coverage. Large numbers of portable instruments have also become available for specialized experiments in particular regions. Seismic records are now far easier to obtain, with centralized archives providing online data access in standard formats.

Earth's average radial velocity and density structures were well established by 1970, including the existence of minor velocity discontinuities near 410- and 660-km depth in the upper mantle. Attention then shifted to resolving lateral differences in velocity structure, first by producing different velocity versus depth profiles for different regions, and more recently by inverting seismic data directly for three-dimensional velocity structures. The latter methods have been given the name "tomography" by analogy to medical imaging techniques. During recent years, tomographic methods of increasing resolution have begun to provide spectacular im-

ages of the structure of Earth's crust and mantle at a variety of scale lengths. Local earthquake tomography at scales from tens of hundreds of kilometers has imaged details of crustal structure in many different regions, including the slow seismic velocities found in sedimentary basins and the sharp velocity changes that can occur near active fault zones.

Figure 1.7 shows seismic velocity perturbations in the mantle, as recently imaged using whole-Earth tomographic methods. Note that the velocity anomalies are strongest at the top and bottom of the mantle, with high velocities beneath the continents in the uppermost mantle and in a ring surrounding the Pacific in the lowermost mantle. Many, but not all, geophysicists ascribe these fast velocities near the core-mantle boundary to the pooling of cold descending slabs from current and past subduction zones around the Pacific. The slow lowermost mantle S velocities seen beneath the south-central Pacific have often been interpreted as a warm region that may feed plumes and oceanic island volcanism, but differences between P and S wave tomography models now indicate that the anomaly is largely compositional in origin (e.g., Masters et al., 2000). Other features include ponding of slabs in the transition zone between the 410 and 660-km discontinuities (see 550 km slice) as well as some evidence for slabs in the midmantle beneath Tonga and South America (see 1000 km slice).

At shallower depths, reflection seismic experiments using controlled sources have led to detailed images of crustal structure, both on land and beneath the oceans (Fig. 1.8). The ability to image three-dimensional structures has greatly expanded the power of seismology to help resolve many outstanding problems in the Earth sciences. These include the structure of fault zones at depth, the deep roots of continents, the properties of mineralogical phase changes in the mantle, the fate of subducting slabs, the structure of oceanic spreading centers, the nature of convection within the mantle, the complicated details of the core-mantle boundary region, and the structure of the inner core.

Most of the preceding discussion is concerned with *structural seismology*, or using records of seismic waves to learn about Earth's internal structure. Progress has also been made in learning about the physics of earthquakes themselves. The turning point came with the investigations following the 1906 San Francisco earthquake. H. F. Reid, an American engineer, studied survey lines across the fault taken before and after the earthquake. His analysis led to the *elastic rebound* theory for the origin of earthquakes in which a slow accumulation of shear stress and strain is suddenly released by movement along a fault. Subsequent work has confirmed that this mechanism is the primary cause of tectonic earthquakes in the crust and is capable of quickly releasing vast amounts of energy. Today, observations of large-scale deformations following large earthquakes, using land- and satellite-based surveying methods, are widely used to constrain the distribution of slip on subsurface faults.

The first widely used measure of earthquake size was the magnitude scale developed for earthquakes in southern California by Charles Richter and Beno Gutenberg in 1935. Because the Richter scale is logarithmic, a small range of Richter magnitudes can describe large variations in earthquake size. The smallest earthquakes that

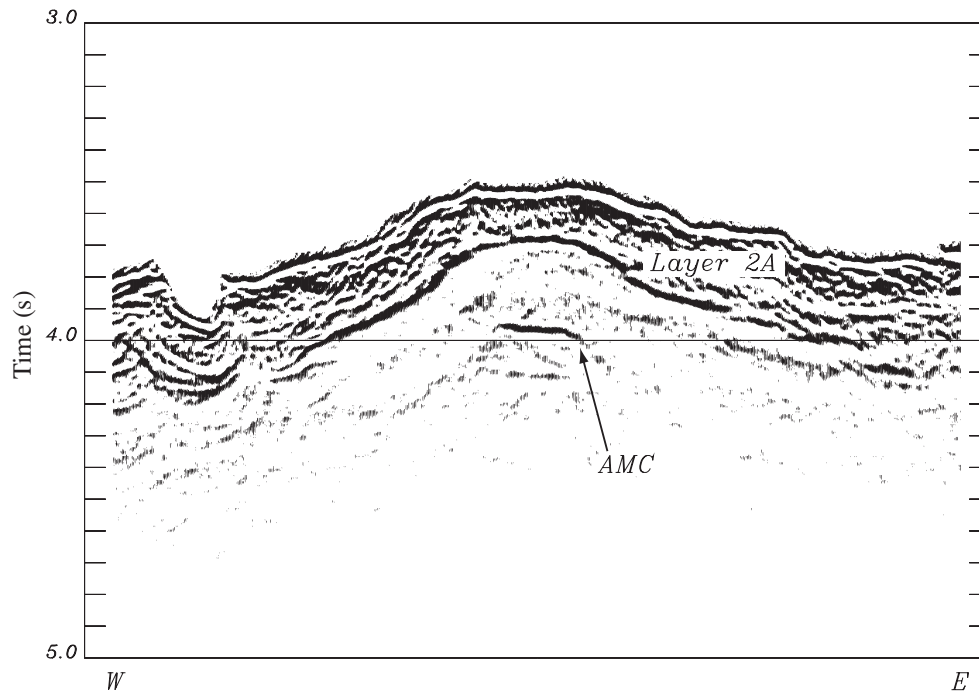


Figure 1.8: An image of the axial magma chamber (AMC) beneath the East Pacific Rise near $14^{\circ}15'S$ obtained through migration processing of reflection seismic data (from Kent et al., 1994). The profile is about 7 km across, with the vertical axis representing the two-way travel time of compressional waves between the surface of the ocean and the reflection point. The sea floor is the reflector at about 3.5 s in the middle of the plot, while the magma chamber appears at about 4.0 s and is roughly 750 m wide. Shallow axial magma chambers are commonly seen beneath fast-spreading oceanic ridges, such as those in the eastern Pacific, but not beneath slow-spreading ridges, such as the Mid-Atlantic Ridge.

are readily felt at the surface have magnitudes of about 3, while great earthquakes such as the 1906 San Francisco earthquake have magnitudes of 8 or greater. A number of different magnitude scales, applicable to different types of seismic observations, have now been developed that are based on Richter's idea. However, most of these scales are empirical and not directly related to properties of the source. A more physically based measure of earthquake size, the *seismic moment*, was formulated by Keiiti Aki in 1966. This led to the definition of the *moment magnitude*, which remains on scale even for the earthquakes of magnitude 8 and greater.

Because catastrophic earthquakes occur rarely in any particular region, humanity often forgets how devastating these events can be. However, history should remind us of their power to suddenly kill tens to thousands of people (see Table 1.1) and of the importance of building earthquake resistant structures. Earth's rapidly increasing population, particularly in cities in seismically active regions, means that future earthquakes may be even more deadly. The great earthquake and tsunami of December 2004 killed over 250,000 people in Sumatra and around the northeast Indian ocean. This earthquake was the first magnitude 9+ earthquake recorded by modern broadband seismographs (instruments were much more primitive for the

Table 1.1: Earthquakes with 70,000 or more deaths.

Year	Location	Magnitude	Deaths
856	Damghan, Iran		200,000
893	Ardabil, Iran		150,000
1138	Aleppo, Syria		230,000
1290	Chihli, China		100,000
1556	Shansi, China	~8	830,000
1667	Shemakha, Caucasia		80,000
1727	Tabriz, Iran		77,000
1755	Lisbon, Portugal	8.7	70,000
1908	Messina, Italy	7.2	~85,000
1920	Gansu, China	7.8	200,000
1923	Kanto, Japan	7.9	143,000
1927	Tsinghai, China	7.9	200,000
1932	Gansu, China	7.6	70,000
1948	Ashgabat, Turkmenistan	7.3	110,000
1976	Tangshan, China	7.5	255,000
2004	Sumatra	9.1	283,106
2005	Pakistan	7.6	86,000
2008	Eastern Sichuan, China	7.9	87,652

Source: http://earthquake.usgs.gov/regional/world/most_destructive.php

1960 Chile and 1964 Alaskan earthquakes). The Sumatra earthquake lasted over 8 minutes and ruptured about 1300 km of fault (see Fig. 1.9). Seismic wave displacements caused by this event were over a centimeter when its surface waves crossed the United States, over 12,000 kilometers away. The radiated seismic energy from this earthquake has been estimated as 1.4 to 3×10^{17} Joules (Kanamori, 2006; Choy and Boatwright, 2007). Normal modes excited by this earthquake could be observed for several months as the Earth continued to vibrate at very long periods.

During the past few decades, large networks of seismometers have been deployed in seismically active regions to map out patterns of earthquake activity, and strong motion instruments have been used to obtain on-scale recordings near large earthquakes. It has become possible to map the time-space history of the slip distribution on faults during major earthquakes. Despite these advances, many fundamental questions regarding the nature of earthquakes remain largely unanswered, including the origin of deep events and the processes by which the rupture of a crustal fault initiates, propagates, and eventually comes to a halt. It is perhaps in these areas of earthquake physics that some of seismology's most important future discoveries remain to be made.

1.2 EXERCISES

1. The radii of the Earth, Moon, and Sun are 6,371 km, 1,738 km, and 6.951×10^5 km, respectively. From Figures 1.1, 1.5, and 1.6, make a rough estimate of how long it takes a P -wave to traverse the diameter of each body.

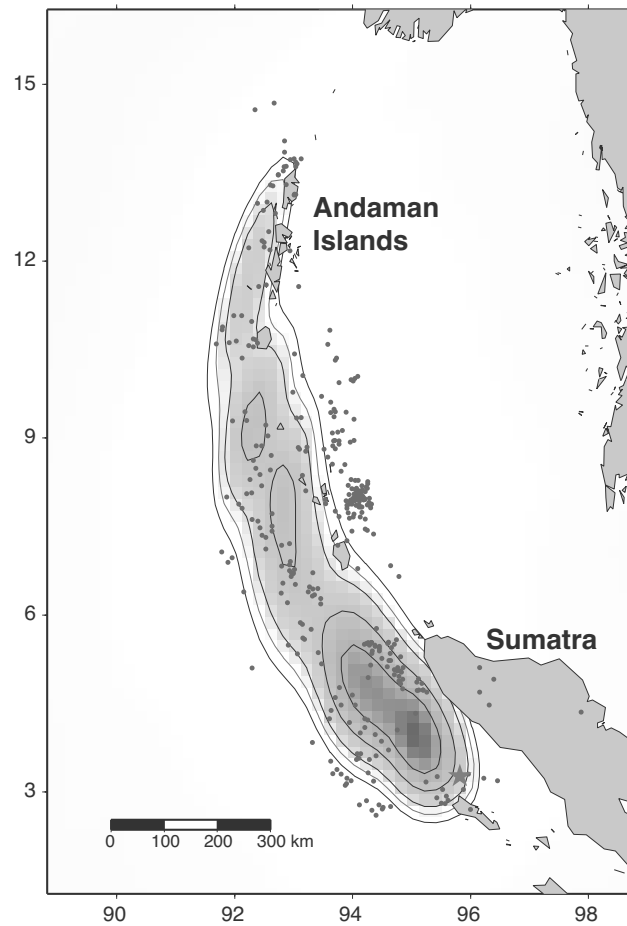


Figure 1.9: The 2004 Sumatra-Andaman earthquake as imaged by Ishii et al. (2005) using high-frequency data from the Japanese Hi-Net array. Note the good agreement between the 1300-km-long rupture zone and the locations of the first 35 days of aftershocks (small dots).

2. Assuming that the P velocity in the ocean is 1.5 km/s, estimate the minimum and maximum water depths shown in Figure 1.8. If the crustal P velocity is 5 km/s, what is the depth to the top of the magma chamber from the sea floor?
3. Assume that the S velocity perturbations plotted at 200 km depth in Figure 1.7 extend throughout the uppermost 300 km of the mantle. Estimate how many seconds earlier a vertically upgoing S -wave will arrive at a seismic station in the middle of Canada, compared to a station in the eastern Pacific. Ignore any topographic or crustal thickness differences between the sites; consider only the integrated travel time difference through the upper mantle.
4. Earthquake moment is defined as $M_0 = \mu DA$, where μ is the shear modulus, D is the average displacement on the fault, and A is the fault area that slipped. The moment of the 2004 Sumatra-Andaman earthquake has been estimated to be about 1.0×10^{23} N m. Assuming that the fault is horizontal, crudely estimate the slip area from the image shown in Figure 1.9. Assuming that the

shear modulus $\mu = 3.0 \times 10^{10} \text{ N/m}^2$, then compute the average displacement on the fault.

5. Do some research on the web and find the energy release of the following: (a) a 1 megaton nuclear explosion, (b) the yearly electricity consumption in the United States, (c) yearly dissipation of tidal energy in Earth's oceans, and (d) the daily energy release of a typical hurricane. Express all your answers in Joules (J) and compare these numbers to the seismic energy release of the 2004 Sumatra earthquake (see text). Note that the total energy release (including heat generated on the fault, etc.) of the Sumatra earthquake may be significantly greater than the seismically radiated energy. This is discussed in Chapter 9.

Chapter 2

Stress and Strain

Any quantitative description of seismic wave propagation or of earthquake physics requires the ability to characterize the internal forces and deformations in solid materials. We now begin a brief review of those parts of stress and strain theory that will be needed in subsequent chapters. Although this section is intended to be self-contained, we will not derive many equations and the reader is referred to any continuum mechanics text (Malvern, 1969, is a classic but there are many others) for further details.

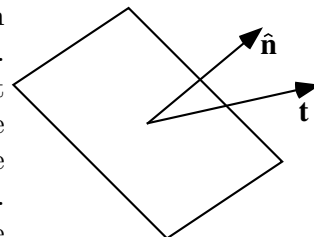
Deformations in three-dimensional materials are termed strain; internal forces between different parts of the medium are called stress. Stress and strain do not exist independently in materials; they are linked through the constitutive relationships that describe the nature of elastic solids.

2.1 The Stress Tensor

Consider an infinitesimal plane of arbitrary orientation within a homogenous elastic medium in static equilibrium. The orientation of the plane may be specified by its unit normal vector, $\hat{\mathbf{n}}$. The force per unit area exerted by the side in the direction of $\hat{\mathbf{n}}$ across this plane is termed the *traction* and is represented by the vector $\mathbf{t}(\hat{\mathbf{n}}) = (t_x, t_y, t_z)$.

If \mathbf{t} acts in the direction shown here, then the traction force is pulling the opposite side toward the interface. This definition is the usual convention in seismology and results in extensional forces being positive and compressional forces being negative. In some other fields, such as rock mechanics, the definition is reversed and compressional forces are positive. There is an equal and opposite force exerted by the side opposing $\hat{\mathbf{n}}$, such that $\mathbf{t}(-\hat{\mathbf{n}}) = -\mathbf{t}(\hat{\mathbf{n}})$. The part of \mathbf{t} which is normal to the plane is termed the *normal stress*, that which is parallel is called the *shear stress*. In the case of a fluid, there are no shear stresses and $\mathbf{t} = -P\hat{\mathbf{n}}$, where P is the pressure.

In general, the magnitude and direction of the traction vector will vary as a function of the orientation of the infinitesimal plane. Thus, to fully describe the internal forces in the medium, we need a general method for determining \mathbf{t} as a



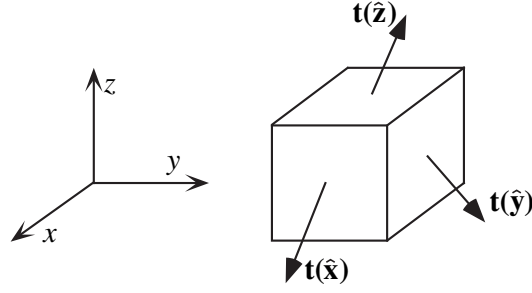


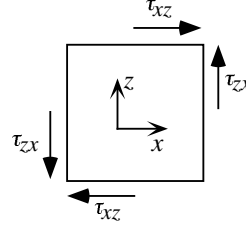
Figure 2.1: The traction vectors $\mathbf{t}(\hat{\mathbf{x}})$, $\mathbf{t}(\hat{\mathbf{y}})$, and $\mathbf{t}(\hat{\mathbf{z}})$ describe the forces on the faces of an infinitesimal cube in a Cartesian coordinate system.

function of $\hat{\mathbf{n}}$. This is accomplished with the *stress tensor*, which provides a linear mapping between $\hat{\mathbf{n}}$ and \mathbf{t} . The stress tensor, $\boldsymbol{\tau}$, in a Cartesian coordinate system (Fig. 2.1) may be defined¹ by the tractions across the yz , xz , and xy planes:

$$\boldsymbol{\tau} = \begin{bmatrix} t_x(\hat{\mathbf{x}}) & t_x(\hat{\mathbf{y}}) & t_x(\hat{\mathbf{z}}) \\ t_y(\hat{\mathbf{x}}) & t_y(\hat{\mathbf{y}}) & t_y(\hat{\mathbf{z}}) \\ t_z(\hat{\mathbf{x}}) & t_z(\hat{\mathbf{y}}) & t_z(\hat{\mathbf{z}}) \end{bmatrix} = \begin{bmatrix} \tau_{xx} & \tau_{xy} & \tau_{xz} \\ \tau_{yx} & \tau_{yy} & \tau_{yz} \\ \tau_{zx} & \tau_{zy} & \tau_{zz} \end{bmatrix}. \quad (2.1)$$

Because the solid is in static equilibrium, there can be no net rotation from the shear stresses. For example, consider the shear stresses in the xz plane. To balance the torques, $\tau_{xz} = \tau_{zx}$. Similarly, $\tau_{xy} = \tau_{yx}$ and $\tau_{yz} = \tau_{zy}$, and the stress tensor $\boldsymbol{\tau}$ is symmetric, that is,

$$\boldsymbol{\tau} = \boldsymbol{\tau}^T = \begin{bmatrix} \tau_{xx} & \tau_{xy} & \tau_{xz} \\ \tau_{xy} & \tau_{yy} & \tau_{yz} \\ \tau_{xz} & \tau_{yz} & \tau_{zz} \end{bmatrix} \quad (2.2)$$



The stress tensor $\boldsymbol{\tau}$ contains only 6 independent elements, and these are sufficient to completely describe the state of stress at a given point in the medium.

The traction across any arbitrary plane of orientation defined by $\hat{\mathbf{n}}$ may be obtained by multiplying the stress tensor by $\hat{\mathbf{n}}$, that is,

$$\mathbf{t}(\hat{\mathbf{n}}) = \boldsymbol{\tau} \hat{\mathbf{n}} = \begin{bmatrix} t_x(\hat{\mathbf{n}}) \\ t_y(\hat{\mathbf{n}}) \\ t_z(\hat{\mathbf{n}}) \end{bmatrix} = \begin{bmatrix} \tau_{xx} & \tau_{xy} & \tau_{xz} \\ \tau_{xy} & \tau_{yy} & \tau_{yz} \\ \tau_{xz} & \tau_{yz} & \tau_{zz} \end{bmatrix} \begin{bmatrix} \hat{n}_x \\ \hat{n}_y \\ \hat{n}_z \end{bmatrix}. \quad (2.3)$$

This can be shown by summing the forces on the surfaces of a tetrahedron (the *Cauchy tetrahedron*) bounded by the plane normal to $\hat{\mathbf{n}}$ and the xy , xz , and yz planes.

The stress tensor is simply the linear operator that produces the traction vector \mathbf{t} from the normal vector $\hat{\mathbf{n}}$, and, in this sense, the stress tensor exists independent of any particular coordinate system. In seismology we almost always write the stress tensor as a 3×3 matrix in a Cartesian geometry. Note that the symmetry

¹Often the stress tensor is defined as the transpose of (2.1) so that the first subscript of $\boldsymbol{\tau}$ represents the surface normal direction. In practice, it makes no difference as $\boldsymbol{\tau}$ is symmetric.

requirement reduces the number of independent parameters in the stress tensor to six from the nine that are present in the most general form of a second-order tensor (scalars are considered zeroth-order tensors, vectors are first order, etc.).

The stress tensor will normally vary with position in a material; it is a measure of the forces acting on infinitesimal planes at each point in the solid. Stress provides a measure only of the forces exerted across these planes and has units of force per unit area. However, other forces may be present (e.g., gravity); these are termed *body forces* and have units of force per unit volume or mass.

2.1.1 Example: Computing the traction vector

Suppose we are given that the horizontal components of the stress tensor are

$$\boldsymbol{\tau} = \begin{bmatrix} \tau_{xx} & \tau_{xy} \\ \tau_{xy} & \tau_{yy} \end{bmatrix} = \begin{bmatrix} -40 & -10 \\ -10 & -60 \end{bmatrix} \text{MPa.}$$

Assuming this is a two-dimensional problem, let us compute the forces acting across a fault oriented at 45° (clockwise) from the x -axis. We typically assume that the x -axis points east and the y -axis points north, so in this case the fault is trending from the northwest to the southeast. To compute the traction vector from equation (2.3), we need the normal vector $\hat{\mathbf{n}}$. This vector is perpendicular to the fault and thus points to the northeast, or parallel to the vector (1,1) in our (x, y) coordinate system. However, remember that $\hat{\mathbf{n}}$ is a *unit* vector and thus we must normalize its length to obtain

$$\hat{\mathbf{n}} = \begin{bmatrix} 1/\sqrt{2} \\ 1/\sqrt{2} \end{bmatrix} = \begin{bmatrix} 0.7071 \\ 0.7071 \end{bmatrix}.$$

Substituting into (2.3), we have

$$\mathbf{t}(\hat{\mathbf{n}}) = \boldsymbol{\tau}\hat{\mathbf{n}} = \begin{bmatrix} -40 & -10 \\ -10 & -60 \end{bmatrix} \begin{bmatrix} 1/\sqrt{2} \\ 1/\sqrt{2} \end{bmatrix} = \begin{bmatrix} -50/\sqrt{2} \\ -70/\sqrt{2} \end{bmatrix} \approx \begin{bmatrix} -35.4 \\ -49.4 \end{bmatrix} \text{MPa.}$$

Note that the traction vector points approximately southwest (see Fig. 2.2). This is the force exerted by the northeast side of the fault (i.e., in the direction of our normal vector) on the southwest side of the fault. Thus we see that there is fault normal compression on the fault. To resolve the normal and shear stress on the fault, we compute the dot products with unit vectors perpendicular ($\hat{\mathbf{n}}$) and parallel ($\hat{\mathbf{f}}$) to the fault

$$\begin{aligned} \mathbf{t}_N &= \mathbf{t} \cdot \hat{\mathbf{n}} = (-50/\sqrt{2}, -70/\sqrt{2}) \cdot (1/\sqrt{2}, 1/\sqrt{2}) = -60 \text{ MPa} \\ \mathbf{t}_S &= \mathbf{t} \cdot \hat{\mathbf{f}} = (-50/\sqrt{2}, -70/\sqrt{2}) \cdot (1/\sqrt{2}, -1/\sqrt{2}) = 10 \text{ MPa} \end{aligned}$$

The fault normal compression is 60 MPa. The shear stress is 10 MPa.

2.1.2 Principal axes of stress

For any stress tensor, it is always possible to find a direction $\hat{\mathbf{n}}$ such that there are no shear stresses across the plane normal to $\hat{\mathbf{n}}$, that is, $\mathbf{t}(\hat{\mathbf{n}})$ points in the $\hat{\mathbf{n}}$ direction.

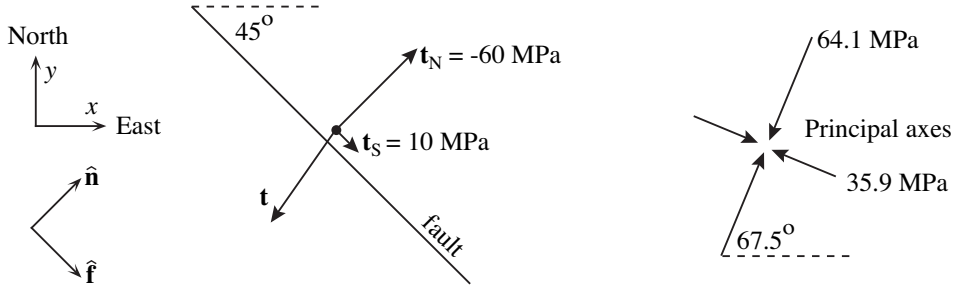


Figure 2.2: The fault tractions and principal stresses for Examples 2.1.1 and 2.1.3.

In this case

$$\begin{aligned} \mathbf{t}(\hat{\mathbf{n}}) &= \lambda \hat{\mathbf{n}} = \boldsymbol{\tau} \hat{\mathbf{n}}, \\ \boldsymbol{\tau} \hat{\mathbf{n}} - \lambda \hat{\mathbf{n}} &= 0, \\ (\boldsymbol{\tau} - \lambda \mathbf{I}) \hat{\mathbf{n}} &= 0, \end{aligned} \quad (2.4)$$

where \mathbf{I} is the identity matrix and λ is a scalar. This is an eigenvalue problem that has a nontrivial solution only when the determinant vanishes

$$\det[\boldsymbol{\tau} - \lambda \mathbf{I}] = 0. \quad (2.5)$$

This is a cubic equation with three solutions, the eigenvalues λ_1 , λ_2 , and λ_3 (do not confuse these with the Lamé parameter λ that we will discuss later). Since $\boldsymbol{\tau}$ is symmetric and real, the eigenvalues are real. Corresponding to the eigenvalues are the eigenvectors $\hat{\mathbf{n}}^{(1)}$, $\hat{\mathbf{n}}^{(2)}$, and $\hat{\mathbf{n}}^{(3)}$. The eigenvectors are orthogonal and define the *principal axes* of stress. The planes perpendicular to these axes are termed the *principal planes*. We can rotate $\boldsymbol{\tau}$ into the $\hat{\mathbf{n}}^{(1)}$, $\hat{\mathbf{n}}^{(2)}$, $\hat{\mathbf{n}}^{(3)}$ coordinate system by applying a similarity transformation (see Appendix B for details about coordinate rotations and transformation tensors):

$$\boldsymbol{\tau}^R = \mathbf{N}^T \boldsymbol{\tau} \mathbf{N} = \begin{bmatrix} \tau_1 & 0 & 0 \\ 0 & \tau_2 & 0 \\ 0 & 0 & \tau_3 \end{bmatrix}, \quad (2.6)$$

where $\boldsymbol{\tau}^R$ is the rotated stress tensor and τ_1 , τ_2 , and τ_3 are the *principal stresses* (identical to the eigenvalues λ_1 , λ_2 , and λ_3). Here \mathbf{N} is the matrix of eigenvectors

$$\mathbf{N} = \begin{bmatrix} n_x^{(1)} & n_x^{(2)} & n_x^{(3)} \\ n_y^{(1)} & n_y^{(2)} & n_y^{(3)} \\ n_z^{(1)} & n_z^{(2)} & n_z^{(3)} \end{bmatrix}, \quad (2.7)$$

with $\mathbf{N}^T = \mathbf{N}^{-1}$ for orthogonal eigenvectors normalized to unit length.

By convention, the three principal stresses are sorted by size, such that $|\tau_1| > |\tau_2| > |\tau_3|$. The maximum shear stress occurs on planes at 45° to the maximum and minimum principle stress axes. In the principal axes coordinate system, one of

these planes has normal vector $\hat{\mathbf{n}} = (1/\sqrt{2}, 0, 1/\sqrt{2})$. The traction vector for the stress across this plane is

$$\mathbf{t}(45^\circ) = \begin{bmatrix} \tau_1 & 0 & 0 \\ 0 & \tau_2 & 0 \\ 0 & 0 & \tau_3 \end{bmatrix} \begin{bmatrix} 1/\sqrt{2} \\ 0 \\ 1/\sqrt{2} \end{bmatrix} = \begin{bmatrix} \tau_1/\sqrt{2} \\ 0 \\ \tau_3/\sqrt{2} \end{bmatrix}. \quad (2.8)$$

This can be decomposed into normal and shear stresses on the plane:

$$\mathbf{t}_N(45^\circ) = \mathbf{t}(45^\circ) \cdot (1/\sqrt{2}, 0, 1/\sqrt{2}) = (\tau_1 + \tau_3)/2 \quad (2.9)$$

$$\mathbf{t}_S(45^\circ) = \mathbf{t}(45^\circ) \cdot (1/\sqrt{2}, 0, -1/\sqrt{2}) = (\tau_1 - \tau_3)/2 \quad (2.10)$$

and we see that the maximum shear stress is $(\tau_1 - \tau_3)/2$.

If $\tau_1 = \tau_2 = \tau_3$, then the stress field is called *hydrostatic* and there are no planes of any orientation in which shear stress exists. In a fluid the stress tensor can be written

$$\boldsymbol{\tau} = \begin{bmatrix} -P & 0 & 0 \\ 0 & -P & 0 \\ 0 & 0 & -P \end{bmatrix}, \quad (2.11)$$

where P is the pressure.

2.1.3 Example: Computing the principal axes

Let us compute the principal axes for our previous example, for which the 2-D stress tensor is given by

$$\boldsymbol{\tau} = \begin{bmatrix} -40 & -10 \\ -10 & -60 \end{bmatrix} \text{ MPa}$$

From equation (2.5), we have

$$\det \begin{bmatrix} -40 - \lambda & -10 \\ -10 & -60 - \lambda \end{bmatrix} = 0$$

or

$$\begin{aligned} (-40 - \lambda)(-60 - \lambda) - (-10)^2 &= 0 \\ \lambda^2 + 100\lambda + 2300 &= 0 \end{aligned}$$

This quadratic equation has roots $\lambda_1 = -64.14$ and $\lambda_2 = -35.86$. Substituting into equation (2.4), we have two eigenvector equations

$$\begin{bmatrix} 24.14 & -10 \\ -10 & 4.14 \end{bmatrix} \begin{bmatrix} n_x^{(1)} \\ n_y^{(1)} \end{bmatrix} = 0 \quad \text{and} \quad \begin{bmatrix} -4.14 & -10 \\ -10 & -24.14 \end{bmatrix} \begin{bmatrix} n_x^{(2)} \\ n_y^{(2)} \end{bmatrix} = 0$$

with solutions for the two eigenvectors (normalized to unit length) of

$$\hat{\mathbf{n}}^{(1)} = \begin{bmatrix} 0.3827 \\ 0.9239 \end{bmatrix} \quad \text{and} \quad \hat{\mathbf{n}}^{(2)} = \begin{bmatrix} -0.9239 \\ 0.3827 \end{bmatrix}.$$

Note that these vectors are orthogonal ($\hat{\mathbf{n}}^{(1)} \cdot \hat{\mathbf{n}}^{(2)} = 0$) and define the principal stress axes. The maximum compressive stress is in the direction $\hat{\mathbf{n}}^{(1)}$, or at an angle to 67.5° with the x -axis (see Fig. 2.2). The eigenvector matrix is

$$\mathbf{N} = \begin{bmatrix} n_x^{(1)} & n_x^{(2)} \\ n_y^{(1)} & n_y^{(2)} \end{bmatrix} = \begin{bmatrix} 0.383 & -0.924 \\ 0.924 & 0.383 \end{bmatrix}$$

which we can use to rotate $\boldsymbol{\tau}$ into the principal stress coordinate system:

$$\begin{aligned} \boldsymbol{\tau}^R = \mathbf{N}^T \boldsymbol{\tau} \mathbf{N} &= \begin{bmatrix} 0.383 & 0.924 \\ -0.924 & 0.383 \end{bmatrix} \begin{bmatrix} -40 & -10 \\ -10 & -60 \end{bmatrix} \begin{bmatrix} 0.383 & -0.924 \\ 0.924 & 0.383 \end{bmatrix} \\ &= \begin{bmatrix} -64.14 & 0 \\ 0 & -35.86 \end{bmatrix} \text{ MPa} \end{aligned}$$

As expected, the principal stresses are simply the eigenvalues, λ_1 and λ_2 . In practice, matrix eigenvector problems are most easily solved using software such as Matlab or Mathematica, or an appropriate computer subroutine. A Matlab script to solve this example is given in the supplemental web material.

2.1.4 Deviatoric stress

Stresses in the deep Earth are dominated by the large compressive stress from the hydrostatic pressure. Often it is convenient to consider only the much smaller *deviatoric* stresses, which are computed by subtracting the mean normal stress (given by the average of the principle stresses, that is $\tau_m = (\tau_1 + \tau_2 + \tau_3)/3$) from the diagonal components of the stress tensor, thus defining the deviatoric stress tensor

$$\boldsymbol{\tau}_D = \begin{bmatrix} \tau_{xx} - \tau_m & \tau_{xy} & \tau_{xz} \\ \tau_{xy} & \tau_{yy} - \tau_m & \tau_{yz} \\ \tau_{xz} & \tau_{yz} & \tau_{zz} - \tau_m \end{bmatrix} \quad (2.12)$$

It should be noted that the trace of the stress tensor is invariant with respect to rotation, so the mean stress τ_m can be computed by averaging the diagonal elements of $\boldsymbol{\tau}$ without computing the eigenvalues (i.e., $\tau_m = (\tau_{11} + \tau_{22} + \tau_{33})/3$). In addition, the deviatoric stress tensor has the same principal stress axes as the original stress tensor.

The stress tensor can then be written as the sum of two parts, the hydrostatic stress tensor $\tau_m \mathbf{I}$ and the deviatoric stress tensor $\boldsymbol{\tau}_D$

$$\boldsymbol{\tau} = \tau_m \mathbf{I} + \boldsymbol{\tau}_D = \begin{bmatrix} -p & 0 & 0 \\ 0 & -p & 0 \\ 0 & 0 & -p \end{bmatrix} + \begin{bmatrix} \tau_{xx} + p & \tau_{xy} & \tau_{xz} \\ \tau_{xy} & \tau_{yy} + p & \tau_{yz} \\ \tau_{xz} & \tau_{yz} & \tau_{zz} + p \end{bmatrix} \quad (2.13)$$

where $p = -\tau_m$ is the mean normal pressure. For isotropic materials (see section 2.3), hydrostatic stress produces volume change without any change in the shape; it is the deviatoric stress that causes shape changes.

Table 2.1: Pressure versus depth inside Earth.

Depth (km)	Region	Pressure (GPa)
0–24	Crust	0–0.6
24–400	Upper Mantle	0.6–13.4
400–670	Transition Zone	13.4–23.8
670–2891	Lower Mantle	23.8–135.8
2891–5150	Outer Core	135.8–328.9
5150–6371	Inner Core	328.9–363.9

2.1.5 Values for stress

Stress has units of force per unit area. In SI units

$$1 \text{ pascal (Pa)} = 1 \text{ N m}^{-2}.$$

Recall that 1 newton (N) = 1 kg m s^{−2} = 10⁵ dyne. Another commonly used unit for stress is the *bar*:

$$\begin{aligned} 1 \text{ bar} &= 10^5 \text{ Pa}, \\ 1 \text{ kbar} &= 10^8 \text{ Pa} = 100 \text{ MPa}, \\ 1 \text{ Mbar} &= 10^{11} \text{ Pa} = 100 \text{ GPa}. \end{aligned}$$

Pressure increases rapidly with depth in Earth, as shown in Table 2.1 using values taken from the reference model PREM (Dziewonski and Anderson, 1981). Pressures reach 13.4 GPa at 400 km depth, 136 GPa at the core–mantle boundary, and 329 GPa at the inner-core boundary. In contrast, the pressure at the center of the Moon is only about 4.8 GPa, a value reached in Earth at 150 km depth (Latham et al., 1969). This is a result of the much smaller mass of the Moon.

These are the hydrostatic pressures inside Earth; shear stresses at depth are much smaller in magnitude and include stresses associated with mantle convection and the dynamic stresses caused by seismic wave propagation. Static shear stresses can be maintained in the upper, brittle part of the crust. Measuring shear stress in the crust is a topic of current research and the magnitude of the stress is a subject of some controversy. Crustal shear stress is probably between about 100 and 1,000 bars (10 to 100 MPa), with a tendency for lower stresses to occur close to active faults (which act to relieve the stress).

2.2 The Strain Tensor

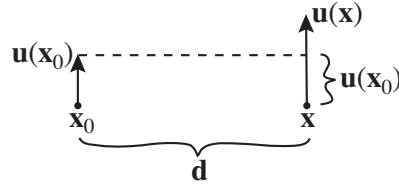
Now let us consider how to describe changes in the positions of points within a continuum. The location of a particular particle at time t relative to its position at a reference time t_0 can be expressed as a vector field, that is, the displacement field \mathbf{u} is given by

$$\mathbf{u}(\mathbf{r}_0, t) = \mathbf{r} - \mathbf{r}_0, \quad (2.14)$$

where \mathbf{r} is the position of the point at time t and \mathbf{x}_0 is the reference location of the point. This approach of following the displacements of particles specified by their original positions at some reference time is called the *Lagrangian description* of motion in a continuum and is almost always the most convenient formulation in seismology.² As we will discuss in chapter 11, seismometers respond to the motion of the particles in the Earth connected to the instrument and thus provide a record of Lagrangian motion. The particle displacement is $\mathbf{u}(t)$, the particle velocity is $\partial\mathbf{u}/\partial t$, and the particle acceleration is $\partial^2\mathbf{u}/\partial t^2$.

The displacement field, \mathbf{u} , is an important concept and we will refer to it often in this book. It is an absolute measure of position changes. In contrast, *strain* is a local measure of relative changes in the displacement field, that is, the spatial gradients in the displacement field. Strain is related to the deformation, or change in shape, of a material rather than any absolute change in position. For example, *extensional strain* is defined as the change in length with respect to length. If a 100 m long string is fixed at one end and uniformly stretched to a length of 101 m, then the displacement field varies from 0 to 1 m along the string, whereas the strain field is constant at 0.01 (1%) everywhere in the string.

Consider the displacement $\mathbf{u} = (u_x, u_y, u_z)$ at position \mathbf{x} , a small distance away from a reference position \mathbf{x}_0 :



We can expand \mathbf{u} in a Taylor series to obtain

$$\mathbf{u}(\mathbf{x}) = \begin{bmatrix} u_x \\ u_y \\ u_z \end{bmatrix} = \mathbf{u}(\mathbf{x}_0) + \begin{bmatrix} \frac{\partial u_x}{\partial x} & \frac{\partial u_x}{\partial y} & \frac{\partial u_x}{\partial z} \\ \frac{\partial u_y}{\partial x} & \frac{\partial u_y}{\partial y} & \frac{\partial u_y}{\partial z} \\ \frac{\partial u_z}{\partial x} & \frac{\partial u_z}{\partial y} & \frac{\partial u_z}{\partial z} \end{bmatrix} \begin{bmatrix} d_x \\ d_y \\ d_z \end{bmatrix} = \mathbf{u}(\mathbf{x}_0) + \mathbf{J}\mathbf{d}, \quad (2.15)$$

where $\mathbf{d} = \mathbf{x} - \mathbf{x}_0$. We have ignored higher order terms in the expansion by assuming that the partials, $\partial u_x/\partial x$, $\partial u_y/\partial x$, etc., are small enough that their products can be ignored (the basis for *infinitesimal strain theory*). Seismology is fortunate that actual Earth strains are almost always small enough that this approximation is valid. We can separate out rigid rotations by dividing \mathbf{J} into symmetric and antisymmetric parts:

$$\mathbf{J} = \begin{bmatrix} \frac{\partial u_x}{\partial x} & \frac{\partial u_x}{\partial y} & \frac{\partial u_x}{\partial z} \\ \frac{\partial u_y}{\partial x} & \frac{\partial u_y}{\partial y} & \frac{\partial u_y}{\partial z} \\ \frac{\partial u_z}{\partial x} & \frac{\partial u_z}{\partial y} & \frac{\partial u_z}{\partial z} \end{bmatrix} = \mathbf{e} + \mathbf{\Omega}, \quad (2.16)$$

²The alternative approach of examining whatever particle happens to occupy a specified location is termed the *Eulerian description* and is often used in fluid mechanics.

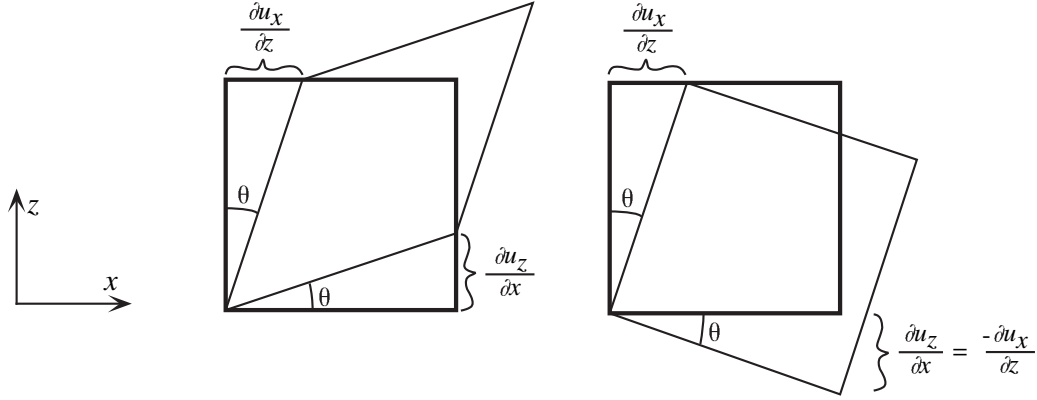


Figure 2.3: The different effects of the strain tensor \mathbf{e} and the rotation tensor $\mathbf{\Omega}$ are illustrated by the deformation of a square in the x - z plane. The off-diagonal components of \mathbf{e} cause shear deformation (left square), whereas $\mathbf{\Omega}$ causes rigid rotation (right square). The deformations shown here are highly exaggerated compared to those for which infinitesimal strain theory is valid.

where the *strain tensor*, \mathbf{e} , is symmetric ($e_{ij} = e_{ji}$) and is given by

$$\mathbf{e} = \begin{bmatrix} \frac{\partial u_x}{\partial x} & \frac{1}{2} \left(\frac{\partial u_x}{\partial y} + \frac{\partial u_y}{\partial x} \right) & \frac{1}{2} \left(\frac{\partial u_x}{\partial z} + \frac{\partial u_z}{\partial x} \right) \\ \frac{1}{2} \left(\frac{\partial u_y}{\partial x} + \frac{\partial u_x}{\partial y} \right) & \frac{\partial u_y}{\partial y} & \frac{1}{2} \left(\frac{\partial u_y}{\partial z} + \frac{\partial u_z}{\partial y} \right) \\ \frac{1}{2} \left(\frac{\partial u_z}{\partial x} + \frac{\partial u_x}{\partial z} \right) & \frac{1}{2} \left(\frac{\partial u_z}{\partial y} + \frac{\partial u_y}{\partial z} \right) & \frac{\partial u_z}{\partial z} \end{bmatrix}, \quad (2.17)$$

and the *rotation tensor*, $\mathbf{\Omega}$, is antisymmetric ($\Omega_{ij} = -\Omega_{ji}$) and is given by

$$\mathbf{\Omega} = \begin{bmatrix} 0 & \frac{1}{2} \left(\frac{\partial u_x}{\partial y} - \frac{\partial u_y}{\partial x} \right) & \frac{1}{2} \left(\frac{\partial u_x}{\partial z} - \frac{\partial u_z}{\partial x} \right) \\ -\frac{1}{2} \left(\frac{\partial u_x}{\partial y} - \frac{\partial u_y}{\partial x} \right) & 0 & \frac{1}{2} \left(\frac{\partial u_y}{\partial z} - \frac{\partial u_z}{\partial y} \right) \\ -\frac{1}{2} \left(\frac{\partial u_x}{\partial z} - \frac{\partial u_z}{\partial x} \right) & -\frac{1}{2} \left(\frac{\partial u_y}{\partial z} - \frac{\partial u_z}{\partial y} \right) & 0 \end{bmatrix}. \quad (2.18)$$

The reader should verify that $\mathbf{e} + \mathbf{\Omega} = \mathbf{J}$.

The effect of \mathbf{e} and $\mathbf{\Omega}$ may be illustrated by considering what happens to an infinitesimal cube (Fig. 2.3). The off-diagonal elements of \mathbf{e} cause shear strain; for example, in two-dimensions, if $\mathbf{\Omega} = \mathbf{0}$ and we assume $\partial u_x / \partial x = \partial u_z / \partial z = 0$, then $\partial u_x / \partial z = \partial u_z / \partial x$, and

$$\mathbf{J} = \mathbf{e} = \begin{bmatrix} 0 & \theta \\ \theta & 0 \end{bmatrix} = \begin{bmatrix} 0 & \frac{\partial u_x}{\partial z} \\ \frac{\partial u_z}{\partial x} & 0 \end{bmatrix}, \quad (2.19)$$

where θ is the angle (in radians, not degrees!) through which each side rotates. Note that the total change in angle between the sides is 2θ .

In contrast, the $\mathbf{\Omega}$ matrix causes rigid rotation, for example, if $\mathbf{e} = \mathbf{0}$, then $\partial u_x / \partial z = -\partial u_z / \partial x$ and

$$\mathbf{J} = \mathbf{\Omega} = \begin{bmatrix} 0 & \theta \\ -\theta & 0 \end{bmatrix} = \begin{bmatrix} 0 & \frac{\partial u_x}{\partial z} \\ \frac{\partial u_z}{\partial x} & 0 \end{bmatrix}. \quad (2.20)$$

In both of these cases there is no volume change in the material. The relative volume increase, or *dilatation*, $\Delta = (V - V_0)/V_0$, is given by the sum of the extensions in the x , y , and z directions:

$$\Delta = \frac{\partial u_x}{\partial x} + \frac{\partial u_y}{\partial y} + \frac{\partial u_z}{\partial z} = \text{tr}[\mathbf{e}] = \nabla \cdot \mathbf{u}, \quad (2.21)$$

where $\text{tr}[\mathbf{e}] = e_{11} + e_{22} + e_{33}$, the *trace* of \mathbf{e} . Note that the dilatation is given by the divergence of the displacement field.

What about the curl of the displacement field? Recall the definition of the curl of a vector field:

$$\nabla \times \mathbf{u} = \left(\frac{\partial u_z}{\partial y} - \frac{\partial u_y}{\partial z} \right) \hat{\mathbf{x}} + \left(\frac{\partial u_x}{\partial z} - \frac{\partial u_z}{\partial x} \right) \hat{\mathbf{y}} + \left(\frac{\partial u_y}{\partial x} - \frac{\partial u_x}{\partial y} \right) \hat{\mathbf{z}}. \quad (2.22)$$

A comparison of this equation with (2.18) shows that $\nabla \times \mathbf{u}$ is nonzero only if $\boldsymbol{\Omega}$ is nonzero and the displacement field contains some rigid rotation.

The strain tensor, like the stress tensor, is symmetric and contains six independent parameters. The *principal axes* of strain may be found by computing the directions $\hat{\mathbf{n}}$ for which the displacements are in the same direction, that is,

$$\mathbf{u} = \lambda \hat{\mathbf{n}} = \mathbf{e} \hat{\mathbf{n}}. \quad (2.23)$$

This is analogous to the case of the stress tensor discussed in the previous section. The three eigenvalues are the *principal strains*, e_1 , e_2 , and e_3 , while the eigenvectors define the principal axes. Note that, except in the case $e_1 = e_2 = e_3$ (*hydrostatic strain*), there is always some shear strain present.

For example, consider a two-dimensional square with extension only in the x direction (Fig. 2.4), so that \mathbf{e} is given by

$$\mathbf{e} = \begin{bmatrix} e_1 & 0 \\ 0 & 0 \end{bmatrix} = \begin{bmatrix} \frac{\partial u_x}{\partial x} & 0 \\ 0 & 0 \end{bmatrix}. \quad (2.24)$$

Angles between lines parallel to the coordinate axes do not change, but lines at intermediate angles are seen to rotate. The angle changes associated with shearing become obvious if we consider the diagonal lines at 45° with respect to the square. If we rotate the coordinate system (see Appendix B) by 45 degrees as defined by the unit vectors $(1/\sqrt{2}, 1/\sqrt{2})$ and $(-1/\sqrt{2}, 1/\sqrt{2})$ we obtain

$$\mathbf{e}' = \begin{bmatrix} 1/\sqrt{2} & 1/\sqrt{2} \\ -1/\sqrt{2} & 1/\sqrt{2} \end{bmatrix} \begin{bmatrix} e_1 & 0 \\ 0 & 0 \end{bmatrix} \begin{bmatrix} 1/\sqrt{2} & -1/\sqrt{2} \\ 1/\sqrt{2} & 1/\sqrt{2} \end{bmatrix} = \begin{bmatrix} e_1/2 & -e_1/2 \\ -e_1/2 & e_1/2 \end{bmatrix} \quad (2.25)$$

and we see that the strain tensor now has off-diagonal terms. As we will see in the next chapter, the type of deformation shown in Figure 2.4 would be produced by a seismic P wave traveling in the x direction; our discussion here shows how P waves involve both compression and shearing.

In subsequent sections, we will find it helpful to express the strain tensor using index notation. Equation (2.17) can be rewritten as

$$e_{ij} = \frac{1}{2}(\partial_i u_j + \partial_j u_i), \quad (2.26)$$

where i and j are assumed to range from 1 to 3 (for the x , y , and z directions) and we are using the notation $\partial_x u_y = \partial u_y / \partial x$.

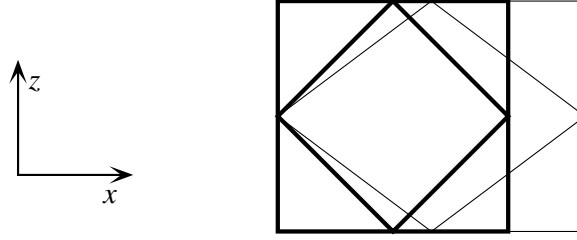


Figure 2.4: Simple extensional strain in the x direction results in shear strain; internal angles are not preserved.

2.2.1 Values for strain

Strain is dimensionless since it represents a change in length divided by length. Dynamic strains associated with the passage of seismic waves in the far field are typically less than 10^{-6} .

2.2.2 Example: Computing strain for a seismic wave

A seismic plane shear wave is traveling through a solid with displacement that can locally be approximated as

$$u_z = A \sin [2\pi f(t - x/c)]$$

where A is the amplitude, f is the frequency and c is the velocity of the wave. What is the maximum strain for this wave?

The non-zero partial derivative from equation (2.17) is

$$\frac{\partial u_z}{\partial x} = \frac{-2\pi f A}{c} \cos [2\pi f(t - x/c)]$$

The maximum occurs when $\cos = -1$ and is thus

$$\left(\frac{\partial u_z}{\partial x} \right)_{max} = \frac{2\pi f A}{c}$$

For example, if $f = 2$ Hz, $c = 3.14$ km/s (3140 m/s) and $A = 1$ mm (10^{-3} m), then $\partial u_z / \partial x(\max) = 4 \times 10^{-6}$ and the strain tensor is given by

$$\epsilon_{max} = \begin{bmatrix} 0 & 0 & 2 \times 10^{-6} \\ 0 & 0 & 0 \\ 2 \times 10^{-6} & 0 & 0 \end{bmatrix}$$

2.3 The Linear Stress-Strain Relationship

Stress and strain are linked in elastic media by a stress-strain or *constitutive* relationship. The most general linear relationship between the stress and strain tensors can be written

$$\tau_{ij} = c_{ijkl} e_{kl} \equiv \sum_{k=1}^3 \sum_{l=1}^3 c_{ijkl} e_{kl}, \quad (2.27)$$

where c_{ijkl} is termed the *elastic tensor*. Here we begin using the *summation convention* in our index notation. Any repeated index in a product indicates that the sum is to be taken as the index varies from 1 to 3. Equation (2.27) is sometimes called the *generalized Hooke's law* and assumes perfect elasticity; there is no energy loss or attenuation as the material deforms in response to the applied stress (sometimes these effects are modeled by permitting c_{ijkl} to be complex). A solid obeying (2.27) is called *linearly elastic*. Non-linear behavior is sometimes observed in seismology (examples include the response of some soils to strong ground motions and the fracturing of rock near earthquakes and explosions) but the non-linearity greatly complicates the mathematics. In this chapter we only consider linearly elastic solids, deferring a discussion of anelastic behavior and attenuation until Chapter 6. Note that stress is not sensitive to the rotation tensor Ω ; stress changes are caused by changes in the volume or shape of solids, as defined by the strain tensor, rather than by rigid rotations.

Equation (2.27) should not be applied to compute the strain for the large values of hydrostatic stress that are present within Earth's interior (see Table 2.1). These strains, representing the compression of rocks under high pressure, are too large for linear stress-strain theory to be valid. Instead, this equation applies to perturbations in stress, termed *incremental stresses*, with respect to an initial state of stress at which the strain is assumed to be zero. This is standard practice in seismology and we will assume throughout this section that stress is actually defined in terms of incremental stress.

The elastic tensor, c_{ijkl} , is a fourth-order tensor with 81 (3^4) components. However, because of the symmetry of the stress and strain tensors and thermodynamic considerations, only 21 of these components are independent. These 21 components are necessary to specify the stress-strain relationship for the most general form of elastic solid. The properties of such a solid may vary with direction; if they do, the material is termed *anisotropic*. In contrast, the properties of an *isotropic* solid are the same in all directions. Isotropy has proven to be a reasonable first-order approximation for much of the Earth's interior, but in some regions anisotropy has been observed and this is an important area of current research (see Section 11.3 for more about anisotropy).

If we assume isotropy (c_{ijkl} is invariant with respect to rotation), it can be shown that the number of independent parameters is reduced to two:

$$c_{ijkl} = \lambda \delta_{ij} \delta_{kl} + \mu (\delta_{il} \delta_{jk} + \delta_{ik} \delta_{jl}), \quad (2.28)$$

where λ and μ are called the *Lamé parameters* of the material and δ_{ij} is the *Kronecker delta* ($\delta_{ij} = 1$ for $i = j$, $\delta_{ij} = 0$ for $i \neq j$). Thus, for example, $C_{1111} = \lambda + 2\mu$, $C_{1112} = 0$, $C_{1122} = \lambda$, $C_{1212} = \mu$, etc. As we shall see, the Lamé parameters, together with the density, will eventually determine the seismic velocities of the material. The stress-strain equation (2.27) for an isotropic solid is

$$\begin{aligned} \tau_{ij} &= [\lambda \delta_{ij} \delta_{kl} + \mu (\delta_{il} \delta_{jk} + \delta_{ik} \delta_{jl})] e_{kl} \\ &= \lambda \delta_{ij} e_{kk} + 2\mu e_{ij}, \end{aligned} \quad (2.29)$$

where we have used $e_{ij} = e_{ji}$ to combine the μ terms. Note that $e_{kk} = \text{tr}[\mathbf{e}]$, the sum of the diagonal elements of \mathbf{e} . Using this equation, we can directly write the components of the stress tensor in terms of the strains:

$$\boldsymbol{\tau} = \begin{bmatrix} \lambda \text{tr}[\mathbf{e}] + 2\mu e_{11} & 2\mu e_{12} & 2\mu e_{13} \\ 2\mu e_{21} & \lambda \text{tr}[\mathbf{e}] + 2\mu e_{22} & 2\mu e_{23} \\ 2\mu e_{31} & 2\mu e_{32} & \lambda \text{tr}[\mathbf{e}] + 2\mu e_{33} \end{bmatrix}. \quad (2.30)$$

The two Lamé parameters completely describe the linear stress-strain relation within an isotropic solid. μ is termed the *shear modulus* and is a measure of the resistance of the material to shearing. Its value is given by half of the ratio between the applied shear stress and the resulting shear strain, that is, $\mu = \tau_{xy}/2e_{xy}$. The other Lamé parameter, λ , does not have a simple physical explanation. Other commonly used elastic constants for isotropic solids include:

Young's modulus E : The ratio of extensional stress to the resulting extensional strain for a cylinder being pulled on both ends. It can be shown that

$$E = \frac{(3\lambda + 2\mu)\mu}{\lambda + \mu}. \quad (2.31)$$

Bulk modulus κ : The ratio of hydrostatic pressure to the resulting volume change, a measure of the incompressibility of the material. It can be expressed as

$$\kappa = \lambda + \frac{2}{3}\mu. \quad (2.32)$$

Poisson's ratio σ : The ratio of the lateral contraction of a cylinder (being pulled on its ends) to its longitudinal extension. It can be expressed as

$$\sigma = \frac{\lambda}{2(\lambda + \mu)}. \quad (2.33)$$

In seismology, we are mostly concerned with the compressional (P) and shear (S) velocities. As we will show later, these can be computed from the elastic constants and the density, ρ :

P velocity, α , can be expressed as

$$\alpha = \sqrt{\frac{\lambda + 2\mu}{\rho}}. \quad (2.34)$$

S velocity, β , can be expressed as

$$\beta = \sqrt{\frac{\mu}{\rho}}. \quad (2.35)$$

Poisson's ratio σ is often used as a measure of the relative size of the P and S velocities; it can be shown that

$$\sigma = \frac{\alpha^2 - 2\beta^2}{2(\alpha^2 - \beta^2)} = \frac{(\alpha/\beta)^2 - 2}{2(\alpha/\beta)^2 - 2}. \quad (2.36)$$

Note that σ is dimensionless and varies between 0 and 0.5 with the upper limit representing a fluid ($\mu = 0$). For a *Poisson solid*, $\lambda = \mu$, $\sigma = 0.25$, and $\alpha/\beta = \sqrt{3}$ and this is a common approximation in seismology for estimating the S velocity from the P velocity and vice-versa. Note that the minimum possible P -to- S velocity ratio for an isotropic solid is $\sqrt{2}$, which occurs when $\lambda = \sigma = 0$. Most crustal rocks have Poisson's ratios between 0.25 and 0.30.

Although many different elastic parameters have been defined, it should be noted that two parameters and density are sufficient to give a complete description of isotropic elastic properties. In seismology, these parameters are often simply the P and S velocities. Other elastic parameters can be computed from the velocities, assuming the density is also known.

2.3.1 Units for elastic moduli

The Lamé parameters, Young's modulus, and the bulk modulus all have the same units as stress (i.e., pascals). Recall that

$$1 \text{ Pa} = 1 \text{ N m}^{-2} = 1 \text{ kg m}^{-1} \text{ s}^{-2}.$$

Note that when this is divided by density (kg m^{-3}) the result is units of velocity squared (appropriate for Equations 2.34 and 2.35).

2.4 EXERCISES

1. Assume that the horizontal components of the 2-D stress tensor are

$$\boldsymbol{\tau} = \begin{bmatrix} \tau_{xx} & \tau_{xy} \\ \tau_{yx} & \tau_{yy} \end{bmatrix} = \begin{bmatrix} -30 & -20 \\ -20 & -40 \end{bmatrix} \text{ MPa}$$

- (a) Compute the normal and shear stresses on a fault that strikes 10° east of north.
 - (b) Compute the principal stresses, and give the azimuths (in degrees east of north) of the maximum and minimum compressional stress axes.
2. The principal stress axes for a 2-D geometry are oriented at $\text{N}45^\circ\text{E}$ and $\text{N}135^\circ\text{E}$, corresponding to principal stresses of -15 and -10 MPa. What are the 4 components of the 2-D stress tensor in a ($x = \text{east}$, $y = \text{north}$) coordinate system?
 3. Figure 2.5 shows a vertical-component seismogram of the 1989 Loma Prieta earthquake recorded in Finland. Make an estimate of the *maximum* strain recorded at this site. Hints: 1 micron = 10^{-6} m, note that the time axis is in 100s of seconds, assume the Rayleigh surface wave phase velocity at the dominant period is 3.9 km/s, remember that strain is $\partial u_z / \partial x$, Table 3.1 may be helpful.

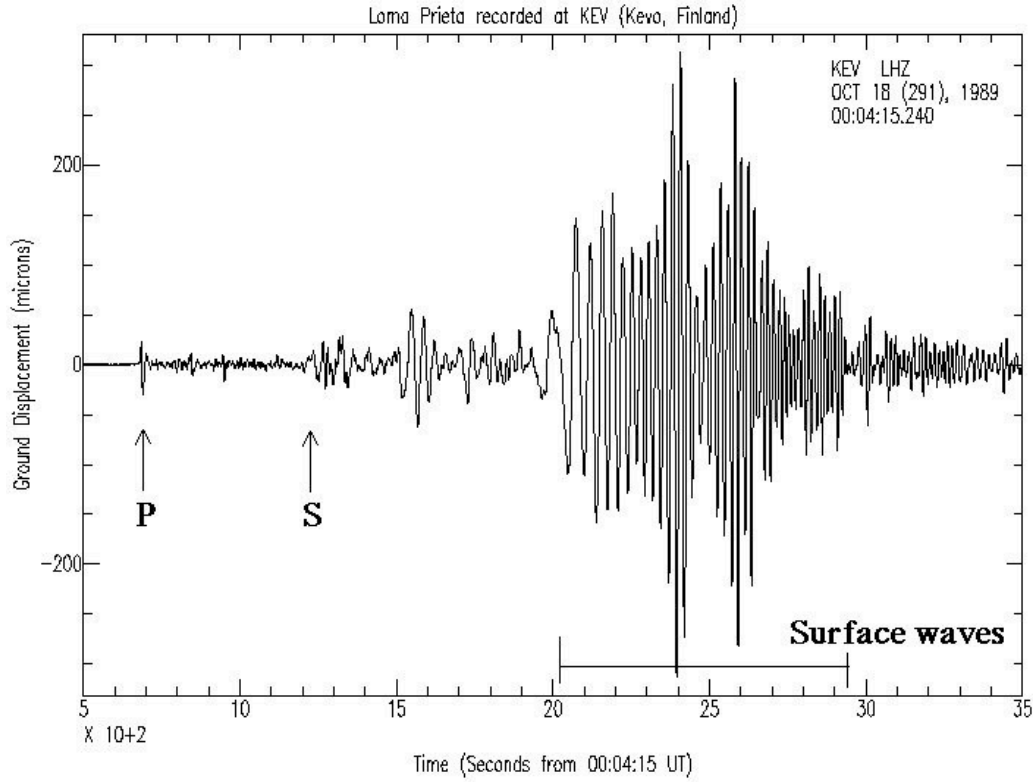


Figure 2.5: A vertical component seismogram of the 1989 Loma Prieta earthquake in California, recorded in Finland. This plot was taken from the Princeton Earth Physics Project, PEPP, website at www.gns.cri.nz/outreach/qt/quaketrackers/curr/seismic_waves.htm.

4. Using Equations (2.4), (2.23), and (2.30), show that the principal stress axes always coincide with the principal strain axes for isotropic media. In other words, show that if \mathbf{x} is an eigenvector of \mathbf{e} , then it is also an eigenvector of $\boldsymbol{\tau}$.
5. From Equations (2.34) and (2.35) derive expressions for the Lamé parameters in terms of the seismic velocities and density.
6. Seismic observations of S velocity can be directly related to the shear modulus μ . However, P velocity is a function of both the shear and bulk moduli. For this reason, sometimes seismologists will compute the *bulk sound speed*, defined as:

$$V_c = \sqrt{\frac{\kappa}{\rho}} \quad (2.37)$$

which isolates the sensitivity to the bulk modulus κ . Derive an equation for V_c in terms of the P and S velocities.

7. What is the P/S velocity ratio for a rock with a Poisson's ratio of 0.30?
8. A sample of granite in the laboratory is observed to have a P velocity of 5.5 km/s and a density of 2.6 Mg/m³. Assuming it is a Poisson solid, obtain values

for the Lamé parameters, Young's modulus, and the bulk modulus. Express your answers in pascals.

9. Using values from the PREM model (Appendix 1), compute values for the bulk modulus on both sides of (a) the core–mantle boundary (CMB) and (b) the inner-core boundary (ICB). Express your answers in pascals.

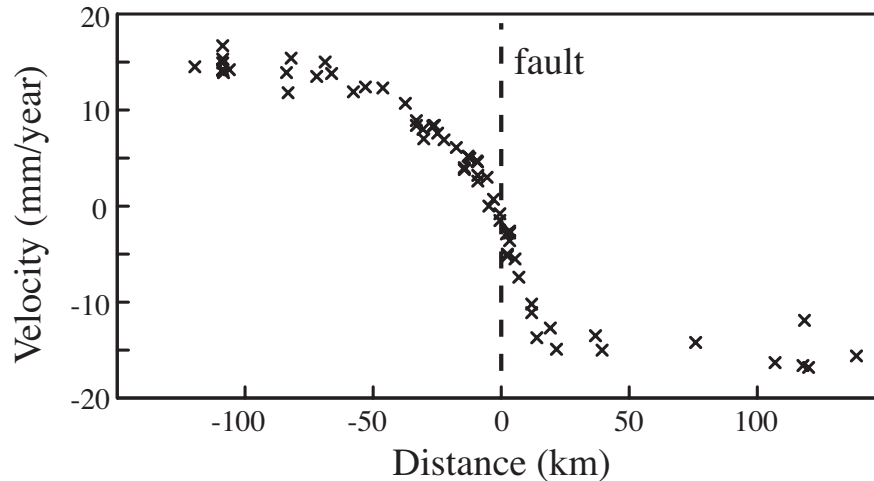


Figure 2.6: Geodetically determined displacement rates near the San Andreas Fault in central California. Velocities are in mm per year for motion parallel to the fault; distances are measured perpendicular to the fault. Velocities are normalized to make the velocity zero at the fault. Data points courtesy of Duncan Agnew.

10. Figure 2.6 shows surface displacement rates as a function of distance from the San Andreas Fault in California.
 - (a) Consider this as a 2-D problem with the x -axis perpendicular to the fault and the y -axis parallel to the fault. From these data, estimate the yearly strain (\mathbf{e}) and rotation ($\mathbf{\Omega}$) tensors for a point on the fault. Express your answers as 2×2 matrices.
 - (b) Assuming the crustal shear modulus is 27 GPa, compute the yearly change in the stress tensor. Express your answer as a 2×2 matrix with appropriate units.
 - (c) If the crustal shear modulus is 27 GPa, what is the shear stress across the fault after 200 years, assuming zero initial shear stress?
 - (d) If large earthquakes occur every 200 years and release all of the distributed strain by movement along the fault, what, if anything, can be inferred about the *absolute* level of shear stress?
 - (e) What, if anything, can be learned about the fault from the observation that most of the deformation occurs within a zone less than 50 km wide?
 - (f) Note: The asymmetry in the deformation pattern is a long-standing puzzle. To learn more, see Schmalzle et al. (2006).

11. Do some research on the observed density of the Sun. Are the high sound velocities in the Sun (see Fig. 1.6) compared to Earth's P velocities caused primarily by low solar densities compared to the Earth, a higher bulk modulus or some combination of these factors?
12. The University of California, San Diego, operates the Piñon Flat Observatory (PFO) in the mountains northeast of San Diego (near Anza). Instruments include high-quality strain meters for measuring crustal deformation.
 - (a) Assume, at 5 km depth beneath PFO, the seismic velocities are $\alpha = 6$ km/s and $\beta = 3.5$ km/s and the density is $\rho = 2.7$ Mg/m³. Compute values for the Lamé parameters, λ and μ , from these numbers. Express your answer in units of pascals.
 - (b) Following the 1992 Landers earthquake ($M_S = 7.3$), located in southern California 80 km north of PFO (Fig. 2.7), the PFO strain meters measured a large static change in strain compared to values before the event. Horizontal components of the strain tensor changed by the following amounts: $e_{11} = -0.26 \times 10^{-6}$, $e_{22} = 0.92 \times 10^{-6}$, $e_{12} = -0.69 \times 10^{-6}$. In this notation 1 is east, 2 is north, and extension is positive. You may assume that this strain change occurred instantaneously at the time of the event. Assuming these strain values are also accurate at depth, use the result you obtained in part (a) to determine the change in stress due to the Landers earthquake at 5 km, that is, compute the change in τ_{11} , τ_{22} , and τ_{12} . Treat this as a two-dimensional problem by assuming there is no strain in the vertical direction and no depth dependence of the strain.
 - (c) Compute the orientations of the principal strain axes (horizontal) for the response at PFO to the Landers event. Express your answers as azimuths (degrees east of north).
 - (d) A steady long-term change in strain at PFO has been observed to occur in which the changes in one year are: $e_{11} = 0.101 \times 10^{-6}$, $e_{22} = -0.02 \times 10^{-6}$, $e_{12} = 0.005 \times 10^{-6}$. Note that the long-term strain change is close to simple E–W extension. Assuming that this strain rate has occurred steadily for the last 1,000 years, from an initial state of zero stress, compute the components of the stress tensor at 5 km depth. (Note: This is probably not a very realistic assumption!) Don't include the large hydrostatic component of stress at 5 km depth.
 - (e) Farmer Bob owns a 1 km² plot of land near PFO that he has fenced and surveyed with great precision. How much land does Farmer Bob gain or lose each year? How much did he gain or lose as a result of the Landers earthquake? Express your answers in m².
 - (f) (COMPUTER) Write a computer program that computes the stress across vertical faults at azimuths between 0 and 170 degrees (east from north, at 10 degree increments). For the stress tensors that you calculated in (b)

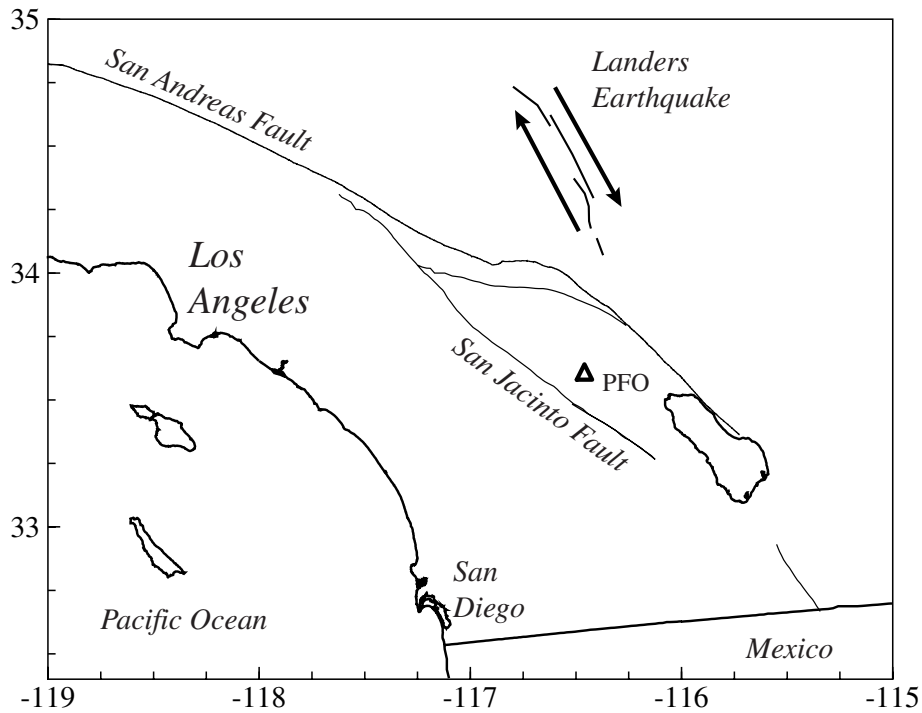


Figure 2.7: The 1992 Landers earthquake ($M_S = 7.3$) in southern California produced measurable strain changes at PFO observatory, located about 80 km south of the event.

and (d), make a table that lists the fault azimuth and the corresponding shear stress and normal stress across the fault (for Landers these are the stress changes, not absolute stresses). At what azimuths are the maximum shear stresses for each case?

- (g) (COMPUTER) Several studies (e.g., Stein et al., 1992, 1994; Harris and Simpson, 1992; Harris et al., 1995; Stein, 1999; Harris, 2002) have modeled the spatial distribution of events following large earthquakes by assuming that the likelihood of earthquake rupture along a fault is related to the *Coulomb failure function* (CFF). Ignoring the effect of pore fluid pressure, the change in CFF may be expressed as:

$$\Delta\text{CFF} = \Delta|\tau_s| + \mu_s\Delta\tau_n,$$

where τ_s is the shear stress (traction), τ_n is the normal stress, and μ_s is the coefficient of static friction (don't confuse this with the shear modulus!). Note that CFF increases as the shear stress increases, and as the compressional stress on the fault is reduced (recall in our sign convention that extensional stresses are positive and compressional stresses are negative). Assume that $\mu_s = 0.2$ and modify your computer program to compute ΔCFF for each fault orientation. Make a table of the

yearly change in ΔCFF due to the long-term strain change at each fault azimuth.

- (h) (COMPUTER) Now assume that the faults will fail when their long-term CFF reaches some critical threshold value. The change in time to the next earthquake may be expressed as

$$\Delta t = \frac{\text{CFF}_{1000+L} - \text{CFF}_{1000}}{\text{CFF}_a},$$

where CFF_a is the annual change in CFF, CFF_{1000} is the thousand year change in CFF, and CFF_{1000+L} is the thousand year + Landers change in CFF (note that $\text{CFF}_{1000+L} \neq \text{CFF}_{1000} + \text{CFF}_L$). Compute the effect of the Landers earthquake in terms of advancing or retarding the time until the next earthquake for each fault orientation. Express your answer in years, using the sign convention of positive time for advancement of the next earthquake and negative time for retardation. (Warning: This is tricky.) Check your answer against the values of shear stress on the fault. Generally (but not always) the earthquake time should advance when the long-term and Landers shear changes agree in sign (either both positive or both negative), and the time should be delayed when the shear stress changes disagree in sign.

- (i) Hint: Getting the signs correct in parts (f)–(h) can be complicated, particularly for part (h). Stresses can be either positive or negative. To help get it right, define two unit vectors for each fault azimuth, one parallel to the fault ($\hat{\mathbf{f}}$) and one perpendicular to the fault ($\hat{\mathbf{p}}$). Compute the traction vector by multiplying the stress tensor by $\hat{\mathbf{p}}$. Then resolve the traction vector into shear stress and normal stress by computing the dot product with $\hat{\mathbf{f}}$ and $\hat{\mathbf{p}}$, respectively. Naturally, $\hat{\mathbf{f}}$ and $\hat{\mathbf{p}}$ must be of unit length for this to work.
- (j) No increase in seismicity (small earthquake activity) has been observed near PFO following the Landers event. Does this say anything about the validity of the threshold CFF model?